Available online at www.sciencedirect.com
ScienceDirect
Trans. Nonferrous Met. Soc. China 35(2025) 3000−3019
Transactions of Nonferrous Metals Society of China
www.tnmsc.cn

Effects of sintering temperature on microstructural evolution and properties of $Co_{1.5}CrFeNi_{1.5}Ti_{0.6}$ high-entropy alloy

Chao WANG[1], Wei-zheng AN[2], Qiang MA[2], Xiang WANG[1], Jia-xin LI[1], Zhao-yang LIANG[1], Qi-dong NIE[3]

1. Key Laboratory of Superlight Materials and Surface Technology, Ministry of Education, Harbin Engineering University, Harbin 150001, China;
2. CNOOC Research Institute Co., Ltd., Beijing 100028, China;
3. Department of Mechanical and Electrical Engineering, Qingdao University of Technology, Linyi 273400, China

Received 3 February 2024; accepted 13 September 2024

Abstract: In order to develop a marine engineering material with excellent mechanical properties and corrosion resistance, a novel non-equiatomic $Co_{1.5}CrFeNi_{1.5}Ti_{0.6}$ high-entropy alloy (HEA) was fabricated through mechanical alloying and spark plasma sintering. The results revealed that the sintering temperature significantly affected the microstructure and phase composition of the HEA owing to the diffusion rate, homogenization, and sluggish diffusion effect of metal atoms. At sintering temperatures below 1050 °C, HEA mainly consisted of face-centered cubic (FCC), Ni_3Ti (ε), $Ni_{2.67}Ti_{1.33}$ (R), and Fe−Cr (σ) phases. The microstructure of alloy comprised coarse dendritic crystals, whose content and size gradually decreased with increasing sintering temperature. However, the HEA sintered above 1100 °C contained only fine equiaxed crystals. HEA sintered at 1100 °C featured only the FCC solid solution, while the ε-phase precipitated at temperatures above 1150 °C. At a sintering temperature of 1050 °C, the alloy microstructure consisted of short rod-like dendrites and fine equiaxed crystals. This alloy achieved the highest yield strength of 1198.71 MPa owing to the effects of precipitation strengthening and grain boundary strengthening. Meanwhile, HEA sintered above 1050 °C exhibited significantly improved corrosion resistance. Considering the microstructure, mechanical, and corrosion properties, 1050 °C was identified as the optimal sintering temperature for $Co_{1.5}CrFeNi_{1.5}Ti_{0.6}$ HEA.

Key words: $Co_{1.5}CrFeNi_{1.5}Ti_{0.6}$ high-entropy alloy; corrosion resistance; microstructure evolution; sintering temperature; strengthening mechanism

1 Introduction

High-entropy alloys (HEAs) exhibit higher strength and improved wear and corrosion resistance than traditional alloys [1−4]. These characteristics make HEAs suitable for applications in marine equipment, high-temperature structures, and wear-resistant coatings [5]. Body-centered cubic (BCC) HEAs composed of Ti, Zr, Nb, and Mo and face-centered cubic (FCC) HEAs with Co, Cr, Fe, and Ni as primary components exhibit high corrosion resistance comparable to or even exceeding that of austenitic stainless steels [6−9]. DIAO et al [10] revealed that BCC HEAs exhibited high strength. However, the limited ductility of BCC HEAs due to their lattice structure restricted their wide application. In contrast, CoCrFeNi HEAs with a single-phase FCC structure achieved 70% elongation, indicating uniform deformation and a high work-hardening capacity [11]. The lower strength and higher ductility of FCC HEAs provided a selective trade-off, enabling the sacrifice of some ductility to enhance strength.

Corresponding author: Xiang WANG, Tel: +86-15776833918, E-mail: wangxiang@hrbeu.edu.cn
https://doi.org/10.1016/S1003-6326(25)66862-2

Various approaches have been used to improve the strength of FCC HEAs. HE et al [12] demonstrated that incorporating Al into $(FeCoNiCrMn)_{100-x}Al_x$ HEAs (x ranging from 0 to 20) modified the crystalline structure from a single FCC phase (x<8) to a duplex FCC and BCC phase (8<x<16), and eventually to a single BCC phase (x>16). With increasing Al content from 0 to 11 at.%, the tensile strength increased from 500 to 1174 MPa, while elongation decreased from 61.7% to 7.7%. ZHU et al [13] developed a near-fully dense CoCrFeNiMn HEA, through selective laser melting. The resulting material achieved a yield strength of 510 MPa. Additionally, FU et al [14] fabricated non-equiatomic $Co_{0.5}FeNiCrTi_{0.5}$ HEA through mechanical alloying (MA) and spark plasma sintering (SPS), resulting in excellent comprehensive mechanical properties and nanophases. Other studies have indicated that non-equiatomic HEAs exhibit higher strength and plasticity than equiatomic HEAs [15−17]. Consequently, non-equiatomic FCC HEAs are highly suitable for high-strength corrosion-resistant applications.

Numerous studies have focused on non-equiatomic CrFeCoNi HEAs. HUANG et al [18] investigated the effect of Co content on the microstructure and mechanical properties of $Co_xCrFeNiTi_{0.3}$ (x=1.0, 0.8, and 0.6) HEAs. The results revealed that higher Co content improved compressive strength and fracture strain. The alloys with Co molar content of 1.0 exhibited the highest strength and plasticity, suggesting that a further increase in Co content could enhance both strength and plasticity. WANG et al [19] investigated $CoCrFeNiTi_x$ HEAs (x=0.1, 0.3, 0.5, and 0.7) and found that the $CoCrFeNiTi_{0.5}$ alloy featured superior corrosion resistance and mechanical properties. The combination of Ti with Co and Ni resulted in a relatively large negative enthalpy of mixing, which facilitated the formation of reinforced phases, such as Ni_3Ti, Ni_2Ti, and $(Co,Ni)_3Ti$, thereby enhancing the hardness and wear resistance of the alloy [11]. This study utilized MA and SPS techniques to prepare non-equiatomic $Co_{1.5}FeNi_{1.5}CrTi_{0.6}$ HEA with increased Co, Ni, and Ti contents, resulting in FCC HEAs reinforced with Ni_3Ti and Ni_2Ti phases.

ASL et al [20] found that the SPS sintering temperature (750−1350 °C) significantly affected the microstructural evolution and mechanical properties of industrial pure Ti. The results indicated that specimens sintered at 1200 °C exhibited the highest mechanical properties and densification. Similarly, ZADRA et al [21] fabricated commercially pure Ti via SPS at temperatures of 700−1150 °C. The results confirmed that excellent microstructure, chemical, and mechanical properties could be achieved at 900 °C. This finding suggests that the sintering temperature in the SPS technique may influence the microstructure and properties of HEAs. However, no studies have yet investigated the effect of SPS sintering temperature on the microstructure and properties, particularly the corrosion properties of CoCrFeNiTi series HEAs. In this study, $Co_{1.5}FeNi_{1.5}CrTi_{0.6}$ HEA samples were fabricated via SPS at temperatures of 950, 1000, 1050, 1100, 1150 and 1200 °C, respectively. The effects of sintering temperature on microstructural evolution, mechanical properties, and corrosion resistance were investigated. The results provide a reference and theoretical basis to further improve and optimize the microstructure and properties of CoCrFeNiTi series HEAs.

2 Experimental

2.1 Alloy preparation

Metal powders of Co, Cr, Fe, Ni and Ti (purity > 99.9 wt.%) were used to prepare mechanically alloyed $Co_{1.5}CrFeNi_{1.5}Ti_{0.6}$ powder according to the compositions listed in Table 1. All metal powders had particle sizes below 70 μm. MA was conducted in a QM−QX planetary mill at 350 r/min using Cr_2O_3 steel balls and vials as grinding media. A ball-to-powder mass ratio of 5∶1 was maintained, and ethanol was added to the MA process to prevent cold welding and metal oxidation. The metal powder was milled for 30 h and then sintered via SPS to produce $Co_{1.5}CrFeNi_{1.5}Ti_{0.6}$ HEA. The SPS process was conducted under the following conditions: current/pause intervals of 50/5 ms, a pressure of 50 MPa, heating and cooling rates of 50 °C/min, a sintering temperature range of 950−1200 °C, and a holding time of 10 min. For analysis, the $Co_{1.5}CrFeNi_{1.5}Ti_{0.6}$ HEA samples sintered at 950, 1000, 1050, 1100, 1150 and 1200 °C were designated as T1, T2, T3, T4, T5 and T6, respectively.

Table 1 Nominal compositions of $Co_{1.5}CrFeNi_{1.5}Ti_{0.6}$ HEA powder (at.%)

Co	Cr	Fe	Ni	Ti
26.78	17.86	17.86	26.78	10.72

2.2 XRD analysis

XRD was performed to determine the phase composition of $Co_{1.5}CrFeNi_{1.5}Ti_{0.6}$ HEA. Data were collected using a Panalytical X-ray diffractometer with a Cu target (λ=0.154 nm). The scan range was 20°−100° at a rate of 5 (°)/min. The interplanar spacing (*d*-spacing) of HEA was calculated from the XRD traces and matched with the relevant crystal structures.

2.3 Microstructure characterization

Microstructure of $Co_{1.5}CrFeNi_{1.5}Ti_{0.6}$ HEA was investigated via scanning electron microscopy (SEM) and energy-dispersive X-ray spectroscopy (EDS). Grain morphology and size distribution were analyzed through electron backscattering diffraction (EBSD). The thickness of the twin layer, nanoparticle size, and volume fraction were estimated using Image J software. Additionally, the microstructure of $Co_{1.5}CrFeNi_{1.5}Ti_{0.6}$ HEA was characterized via transmission electron microscopy (TALOS G2 F200X) and selected area electron diffraction (SAED).

2.4 Mechanical property measurement

Uniaxial compression tests were performed at room temperature using a testing machine (INSTRON 68MT−50) with a strain rate of 5×10^{-4} s^{-1}. The compression specimens had dimensions of 4 mm × 4 mm × 8 mm. Hardness was measured using a Vickers hardness tester (HUAYIN) with a load of 500 g and a holding time of 15 s. Twelve replicate tests were conducted for each specimen. Compression fracture morphology was examined via SEM.

2.5 Electrochemical test

Potentiodynamic polarization test was conducted on HEA in a 3.5 wt.% NaCl solution using an electrochemical potentiostat (CHI700E). Electrochemical measurement was conducted with a conventional three-electrode. A saturated calomel electrode (SCE) and a platinum foil served as the reference electrode and the counter electrode, respectively. The HEA specimen with an exposed area of 100 mm^2 was used as the working electrode. Open circuit potential (OCP) was measured for 1200 s before the polarization tests to achieve a nearly stable rest potential. Each specimen was scanned at a rate of 1 mV/s from an initial potential of −150 mV versus OCP to a final potential of 1.5 V (vs SCE). The composition of the surface oxides was analyzed via X-ray photoelectron spectroscopy (XPS, ESCALAB 250Xi).

3 Results

3.1 Phase composition

The equilibrium phase diagram of $Co_{1.5}CrFeNi_{1.5}Ti_{0.6}$ HEA was simulated using the CALPHAD software (Thermo-Calc) (Fig. 1(a)). The $Co_{1.5}CrFeNi_{1.5}Ti_{0.6}$ HEA contained σ, Ni_3Ti, FCC, Laves and BCC phases. To significantly enhance strength and maintain good plasticity and corrosion resistance, it is crucial to reduce the content of BCC and σ phases, and increase the Ni_3Ti content [22−24]. Although there is a significant

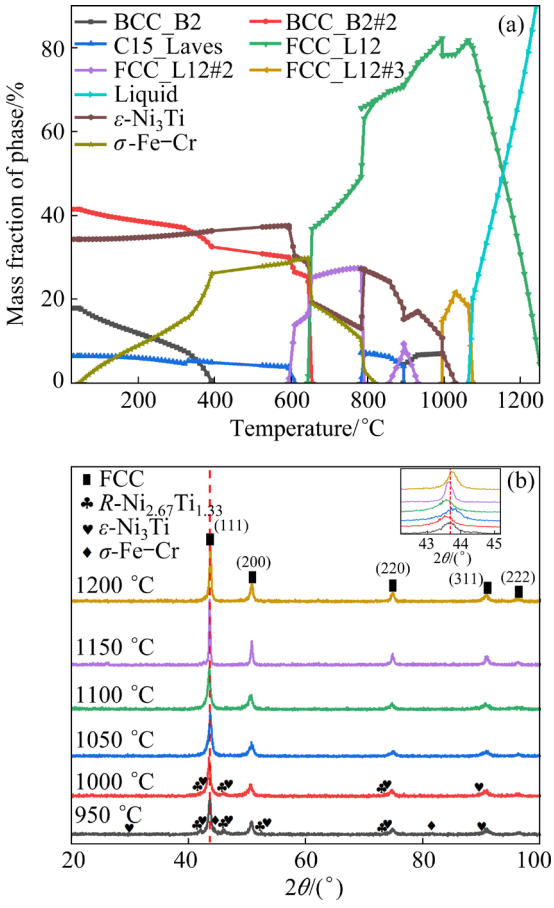

Fig. 1 Equilibrium phase diagram (a) and XRD patterns (b) of $Co_{1.5}CrFeNi_{1.5}Ti_{0.6}$ HEA at different sintering temperatures

amount of Ni_3Ti at 800−1000 °C, ensuring the crystallinity of the block after plasma sintering is more crucial for assessing the overall performance of HEAs. Therefore, the sintering temperature was set within the range of 950−1200 °C.

Figure 1(b) presents the XRD patterns of $Co_{1.5}CrFeNi_{1.5}Ti_{0.6}$ HEA samples fabricated via MA and SPS techniques. The patterns revealed narrow and sharp peaks, indicating the high crystallinity of HEAs sintered at 950−1200 °C. The $Co_{1.5}CrFeNi_{1.5}Ti_{0.6}$ HEA mainly comprised the FCC matrix phase (a solid solution with a $Co_{1.5}CrFeNi_{1.5}Ti_{0.6}$ structure), Ni_3Ti type ε-phase (an intermetallic compound with a hexagonal structure, a=5.096 Å, c=8.304 Å, c/a=1.63), $Ni_{2.67}Ti_{1.33}$ type R-phase (an intermetallic compound with a Ni−Ti system, a=2.579 Å, c=44.162 Å, c/a=17.12), and Fe−Cr type σ-phase (a disordered solid solution with a BCC structure, a=8.845 Å, c=4.567 Å, c/a=0.52) [25,26]. With increasing sintering temperature, the intensity of the diffraction peaks for the FCC phase increased, while those for the σ, ε, and R phases decreased (Fig. 1(b)). This indicates a gradual increase in the FCC phase content in $Co_{1.5}CrFeNi_{1.5}Ti_{0.6}$, with a corresponding decrease in the σ, ε, and R phases. At sintering temperatures above 1050 °C, the diffraction peaks for the σ, ε, and R phases were not detected, owing to their low content in the alloys. The lattice constant of the FCC phase in the alloy was calculated using the intergranular spacing formula and Bragg's equation [27] (Table 2). The lattice constant of the FCC phase significantly varied at different sintering temperatures, suggesting considerable alteration in the microstructure of $Co_{1.5}CrFeNi_{1.5}Ti_{0.6}$ HEA [28]. The variation in the lattice constant was mainly attributed to the solid solution of ε, R, and σ phases and the precipitation of ε-phase nanoparticles.

Table 2 Lattice constant of FCC phase in $Co_{1.5}CrFeNi_{1.5}Ti_{0.6}$ HEA (Å)

T1	T2	T3	T4	T5	T6
3.584	3.593	3.585	3.592	3.587	3.584

3.2 Microscopic morphology

Figure 2 shows the microstructure of $Co_{1.5}CrFeNi_{1.5}Ti_{0.6}$ HEA samples fabricated at different sintering temperatures. At lower sintering temperatures (950 and 1000 °C), the alloy exhibited a typical coarse dendrite microstructure (Figs. 2(a) and (b)). Both the content and size of the dendrites gradually decreased with increasing sintering temperature. At 1050 °C, the microstructure exhibited numerous short rod-like dendrites (Fig. 2(c)) and fine equiaxed crystals (Fig. 2(c_1)). These rod-like dendrites were unevenly distributed within the matrix, which also contained numerous nanoparticles (the inset in Fig. 2(c_1)). At a sintering temperature of 1100 °C, the alloy mainly comprised finely equiaxed grains (Figs. 2(d) and 2(d_1)) and exhibited a nearly single FCC phase structure, with only a few particles along the grain boundaries. At 1150 and 1200 °C, the alloy retained the finely equiaxed grains, with numerous nanoparticles dispersed throughout the matrix (Figs. 2(e, f), and their insets). However, as the sintering temperature exceeded 1150 °C, a small amount of metal liquid leaked from the graphite mold. This leakage altered the alloy composition and damaged the graphite abrasives, indicating that the sintering temperature of the alloy should be limited to 1150 °C.

Figure 3 shows SEM image and EDS analysis of the dendritic (DR) region, and the EDS results are presented in Table 3. The chemical composition and elemental distribution in both DR and interdendritic (ID) zones revealed a uniform distribution of Co throughout the alloy. Moreover, the DR region exhibited significant enrichment in Ti and Ni, with its chemical composition closely similar to those of Ni_2Ti and Ni_3Ti. XRD analysis confirmed the presence of the R-phase and ε-phase in the DR region [11,26]. In contrast, the ID regions comprised the FCC matrix phase, σ-phase, and white blocky nanoparticles. The absence of Fe and Cr in the DR region led to their segregation into the ID region, forming the σ-phase [11,29].

The micromorphology and size statistics of nanoparticles are shown in Fig. 4. The size of the nanoparticles decreased with increasing sintering temperature. At lower temperatures (950 and 1000 °C), the nanoparticles exhibited uneven sizes and distributions, mainly concentrated in the ID region, with average sizes of 66.49 and 54.90 nm, respectively. The nanoparticles sintered at 1050 °C exhibited a more uniform distribution, with an average size of 55.05 nm. At a sintering temperature of 1100 °C, no nanoparticles were visible in the matrix, although some areas still contained few nano-

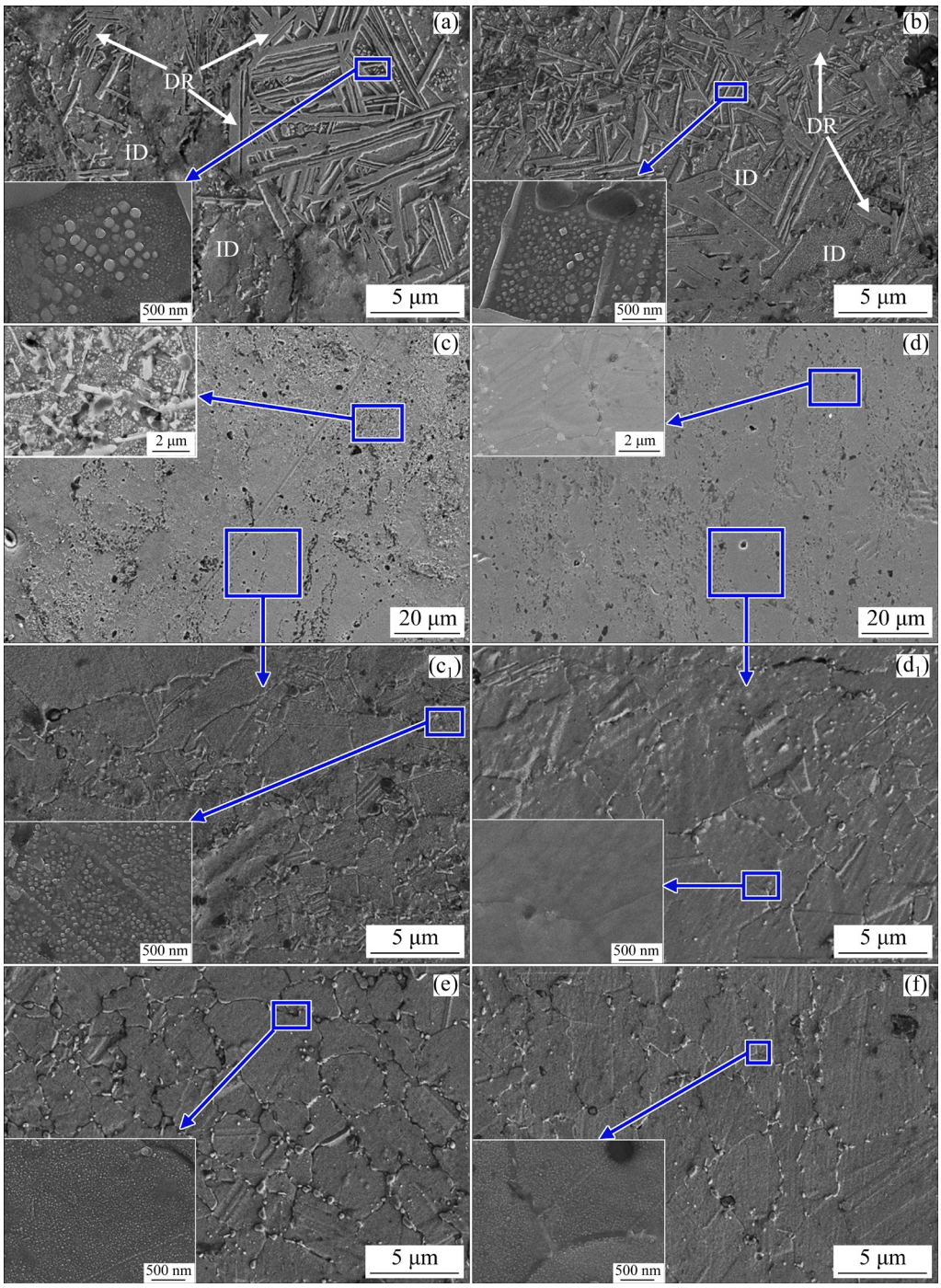

Fig. 2 SEM images of $Co_{1.5}CrFeNi_{1.5}Ti_{0.6}$ HEA sintered at different sintering temperatures: (a) 950 °C; (b) 1000 °C; (c, c_1) 1050 °C; (d, d_1) 1100 °C; (e) 1150 °C; (f) 1200 °C

particles, likely owing to composition inhomogeneity. However, as the sintering temperature exceeded 1150 °C, the nanoparticles reprecipitated within the matrix, resulting in a uniform distribution and smaller size, with none of the particles exceeding 26 nm.

To further investigate the microstructure of $Co_{1.5}CrFeNi_{1.5}Ti_{0.6}$ HEA and the crystal structure of the nanoparticles, the alloy sintered at 1050 °C was extensively analyzed via TEM. The results are shown in Fig. 5. The SAED pattern along the [100] zone axis (denoted by the red arrow) and the [211] zone axis (indicated by the yellow arrow) in Fig. 5(a_1) confirmed that the alloy comprised an FCC matrix and ε nanoparticle phases. The SAED pattern revealed superlattice reflections, indicating

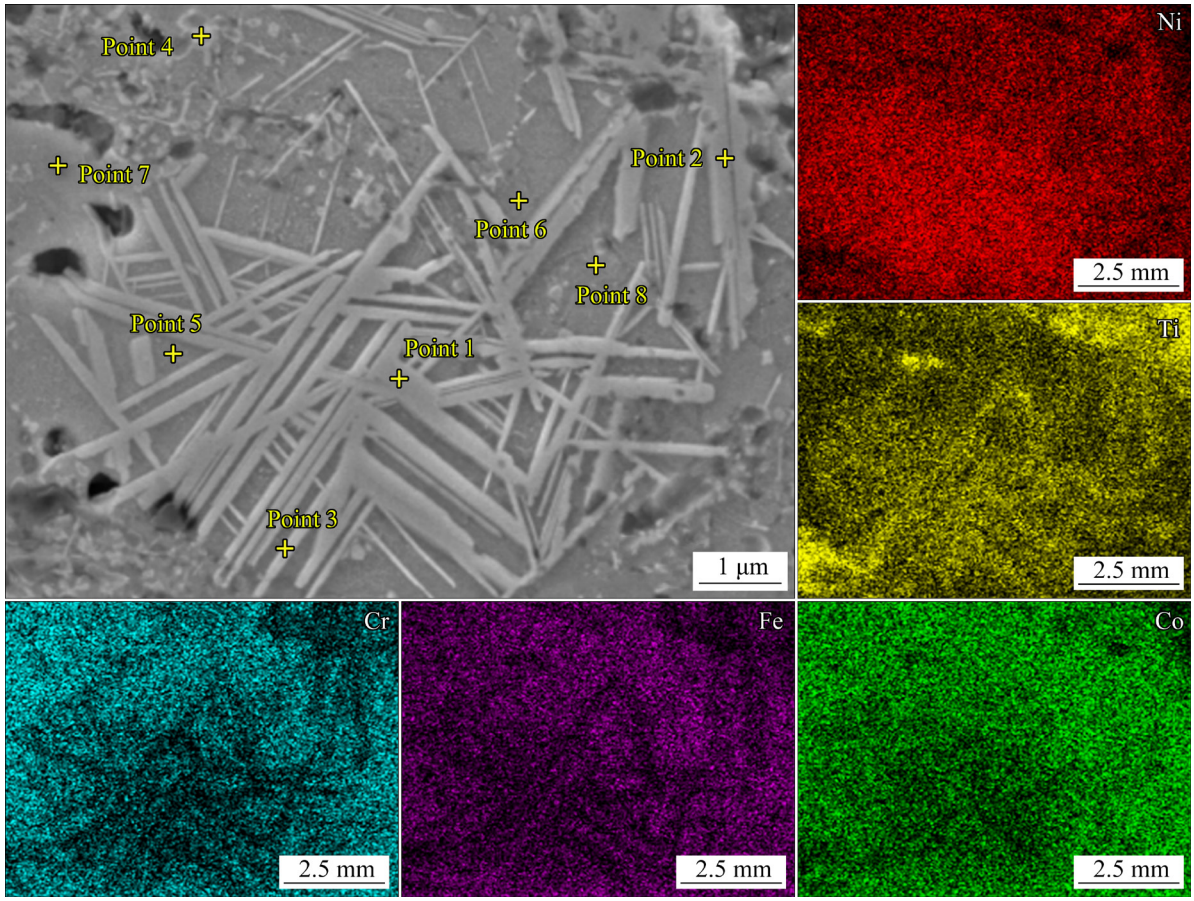

Fig. 3 SEM image and EDS mappings of DR region

Table 3 Chemical compositions of DR and ID zones in Fig. 3 for $Co_{1.5}CrFeNi_{1.5}Ti_{0.6}$ HEA (at.%)

Zone	Phase	Point	Co	Cr	Fe	Ni	Ti
DR	*R*	1	26.07	3.97	8.09	38.07	23.8
		2	26.73	3.17	6.35	38.48	25.27
	ε	3	14.61	5.84	9.87	53.33	16.34
		4	17.09	10.55	9.03	48.2	15.13
ID	*σ*	5	23.05	21.17	32.28	17.38	6.12
		6	26.49	19.66	30.85	18.42	4.59
	FCC	7	31.73	16.71	9.76	29.78	12.01
		8	34.14	18.96	12.39	24.73	9.78
Nominal composition			26.78	17.86	17.86	26.78	10.72

that the *ε*-phase had the hexagonal close-packed (HCP) structure of Ni_3Ti (denoted by the yellow arrow) [30−32]. The alloy exhibited significant lattice distortion and contained some twins (Figs. 5(b, c)).

The EBSD characterization of $Co_{1.5}CrFeNi_{1.5}Ti_{0.6}$ HEA fabricated at different sintering temperatures is shown in Fig. 6. As the sintering temperature increased from 950 to 1150 °C, the grain size of the FCC matrix phase first increased, reaching a maximum at 1100 °C, and then decreased as the temperature continuously increased to 1150 °C (Figs. 6(a_2−f_2)). At 1200 °C, grain coarsening occurred, and the grain size increased to 2.31 μm. Moreover, the grains contained numerous twins owing to the stacking fault energy of the alloy (Figs. 6(a−f)) [30,33]. The volume fraction of these twins is presented in Table 4.

3.3 Mechanical properties

Table 5 shows the variations in the Vickers hardness of $Co_{1.5}CrFeNi_{1.5}Ti_{0.6}$ HEA with increasing sintering temperature. Notably, at a sintering temperature of 1050 °C, the alloy achieved the highest hardness of $HV_{0.5}$ 492.0, which was 3.2 times that of conventional ocean engineering austenitic stainless steel SUS316L ($HV_{0.5}$ 155.6) and twice that of dual-phase stainless steel SAF2507 ($HV_{0.5}$ 246.0).

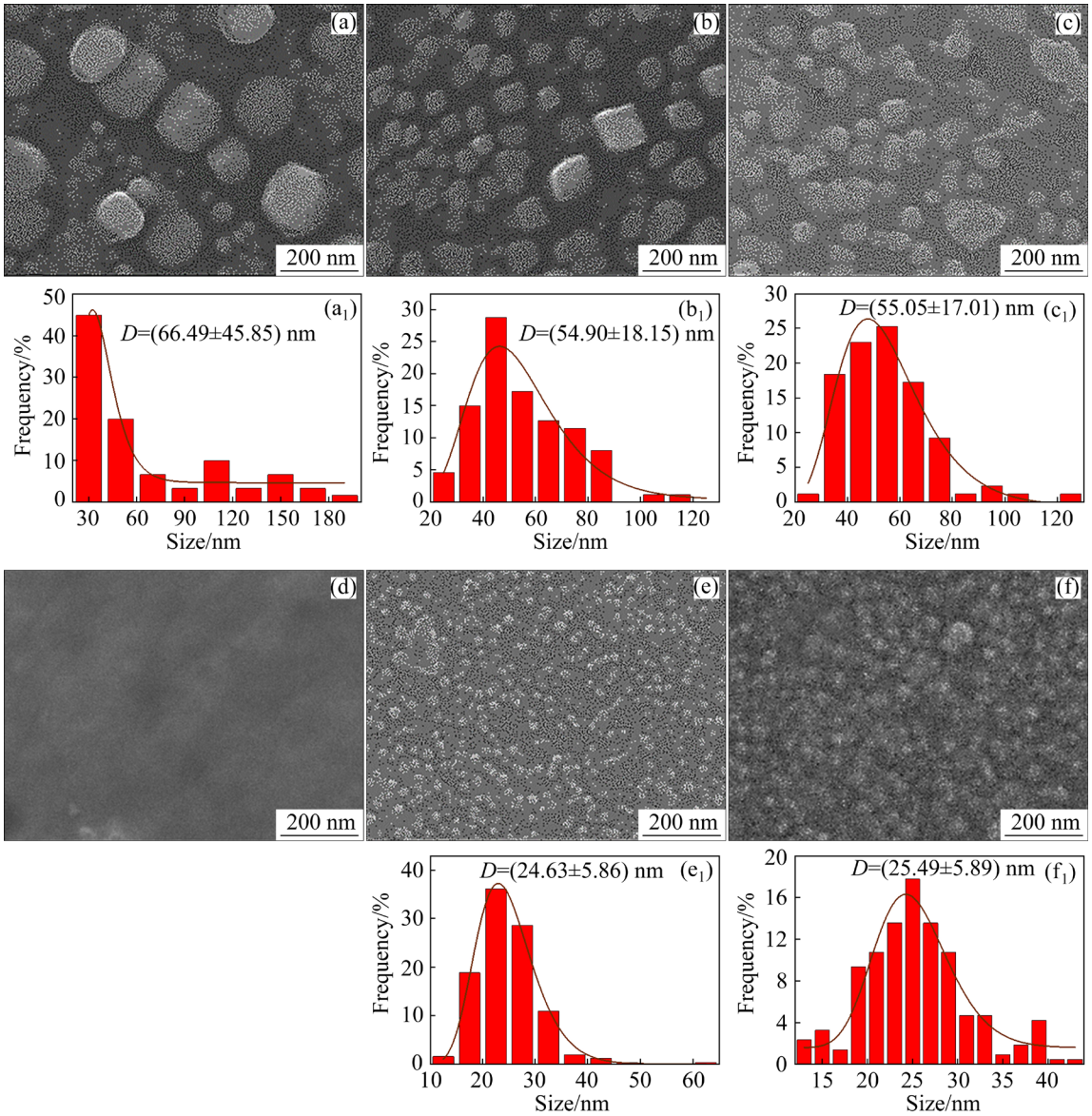

Fig. 4 High-resolution SEM images (a–f) and size statistics of nanoparticles (a_1–c_1, e_1, f_1) of $Co_{1.5}CrFeNi_{1.5}Ti_{0.6}$ HEA sintered at different temperatures: (a, a_1) 950 °C; (b, b_1) 1000 °C; (c, c_1) 1050 °C; (d) 1100 °C; (e, e_1) 1150 °C; (f, f_1) 1200 °C

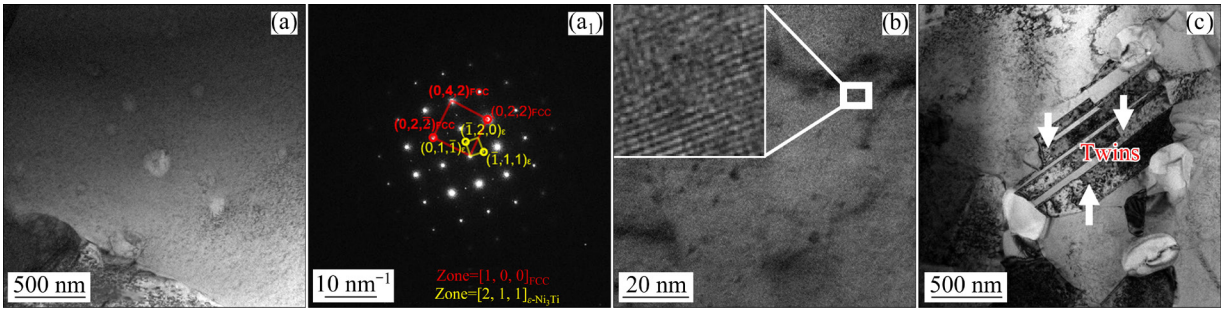

Fig. 5 TEM images and SAED pattern of $Co_{1.5}CrFeNi_{1.5}Ti_{0.6}$ HEA at 1050 °C: (a, a_1) Bright-field image with SAED patterns of FCC [100] and HCP [211] zone axis, respectively; (b) Lattice distortion; (c) Bright-field image of twins

Figure 7 presents the compressive engineering stress–strain curves of $Co_{1.5}CrFeNi_{1.5}Ti_{0.6}$ HEA. The corresponding mechanical properties are listed in Table 5. The compressive strain of the alloys gradually increased with increasing sintering temperature. The alloy sintered at 1150 °C exhibited

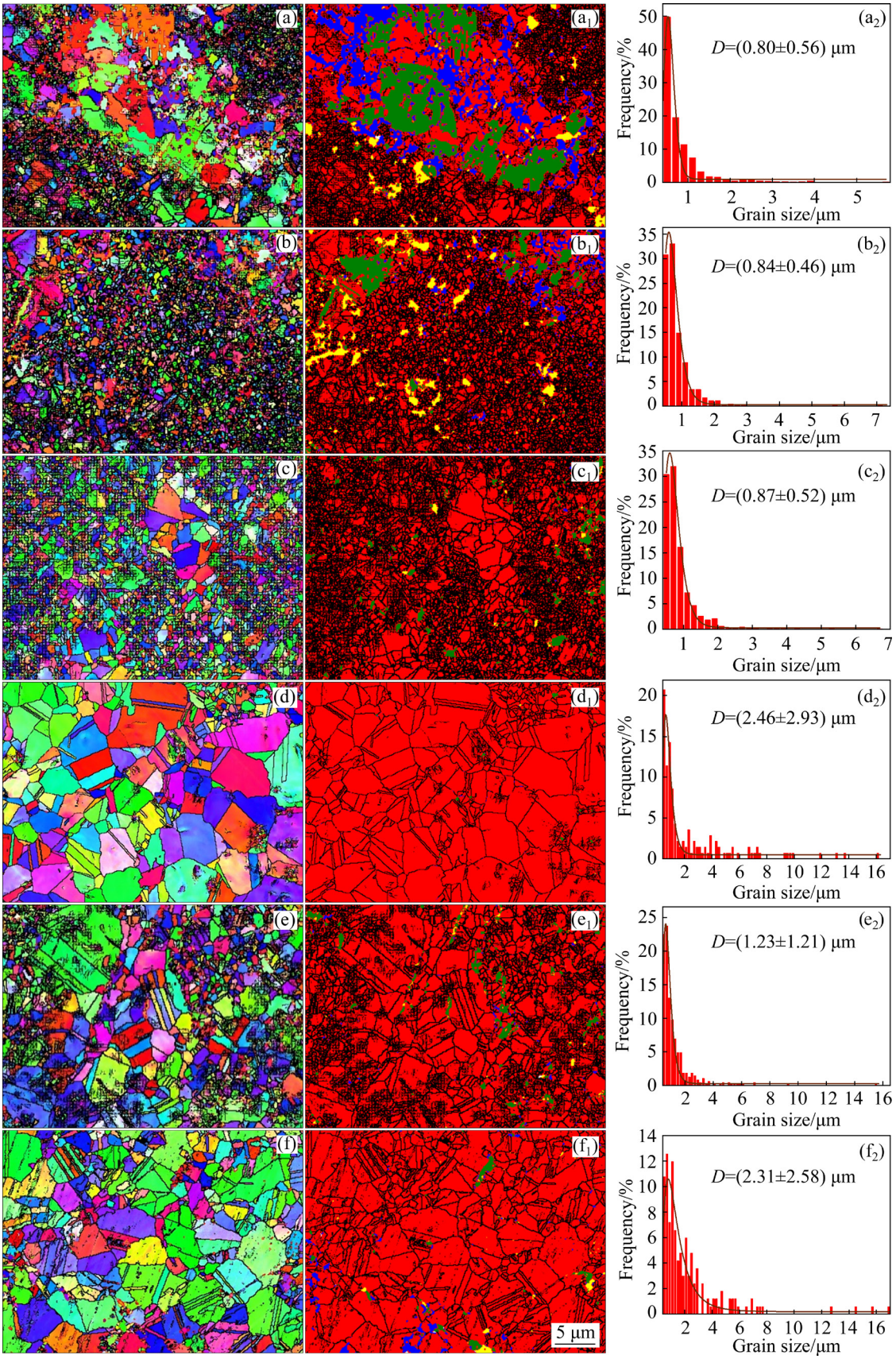

Fig. 6 EBSD characterization of $Co_{1.5}CrFeNi_{1.5}Ti_{0.6}$ HEA fabricated at different sintering temperatures: (a, a_1, a_2) 950 °C; (b, b_1, b_2) 1000 °C; (c, c_1, c_2) 1050 °C; (d, d_1, d_2) 1100 °C; (e, e_1, e_2) 1150 °C; (f, f_1, f_2) 1200 °C; (a−f) Inverse pole figure (IPF) maps; (a_1−f_1) Phase distribution maps (red−FCC, blue−σ, green−R, yellow−ε); (a_2−f_2) Grain size statistics of FCC matrix phase

Table 4 Volume fraction of twins in $Co_{1.5}CrFeNi_{1.5}Ti_{0.6}$ HEA (%)

T1	T2	T3	T4	T5	T6
4.58	3.67	16.3	19.1	12.0	14.8

the highest compressive strength of 1880.40 MPa. However, while the alloy was sintered at 1050 °C, the highest yield strength of 1198.71 MPa was achieved, with its compressive strength only slightly lower than that of the alloy sintered at 1150 °C. In practical engineering applications, yield strength more accurately indicates material deformability and toughness compared with compressive strength. Considering the hardness, yield strength, compressive strength, and plasticity, a sintering temperature of 1050 °C was considered optimal for $Co_{1.5}CrFeNi_{1.5}Ti_{0.6}$ HEA.

Figures 8(a−f) show the macromorphology of the fracture surfaces for $Co_{1.5}CrFeNi_{1.5}Ti_{0.6}$ HEA. The fracture surfaces of all samples were inclined at ~45° to the stress axis, indicating typical brittle fracture behavior. At low sintering temperatures, the compressed samples exhibited minimal deformation, with relatively flat structures. As the sintering temperature increased, the samples exhibited greater deformation owing to the improved plasticity of HEAs. Figures 8(a_1−f_1) display the micromorphology of the fracture surfaces for HEA. All samples exhibited cleavage steps (denoted by white arrows in Figs. 8(a_1–f_1) and numerous "river" patterns (indicated by yellow arrows in Figs. 8(a_1−f_1). The fracture surface featured a relatively flat morphology, indicating a brittle quasi-cleavage fracture.

3.4 Electrochemical corrosion property

Figure 9 shows the potential polarization curves of $Co_{1.5}FeCrNi_{1.5}Ti_{0.6}$ HEA in a 3.5 wt.% NaCl solution. Because 1200 °C was considered excessively high for alloy sintering, it was not discussed in the subsequent section. The self-corrosion potentials (φ_{corr}) and self-corrosion current densities (J_{corr}) of the alloys were determined from Fig. 9 using Tafel linear extrapolation, and the results are presented in Table 6. At lower sintering temperatures (950 and 1000 °C), the φ_{corr} of the alloy was more than twice that of the alloys sintered at other temperatures, indicating a greater tendency for self-corrosion. As the sintering temperature exceeded 1050 °C, the φ_{corr} significantly increased, leading to a substantial improvement in the corrosion resistance of the alloy. Particularly, the alloy sintered at 1050 °C exhibited the lowest J_{corr} and self-corrosion tendency, indicating higher corrosion resistance than other samples. Moreover, this comparison indicates that the corrosion resistance of the alloy sintered at 1050 °C was intermediate between that of stainless steels SAF2507 and SUS316L.

To elucidate the differences in the corrosion resistance of $Co_{1.5}FeCrNi_{1.5}Ti_{0.6}$ HEAs sintered at different temperatures, the passivation film composition of HEAs was analyzed via XPS. The detailed spectra of Ti $2p_{3/2}$, Cr $2p_{3/2}$, Fe $2p_{3/2}$, Ni $2p_{3/2}$, Co $2p_{3/2}$, and O 1s were fitted and analyzed (Figs. 10 and 11).

The XPS spectra of the passivation film revealed a mixture of metallic Ti^0 and TiO_2 on the alloy surface, with binding energies of 453.8 and 458.5 eV, respectively (Figs. 10(a−a_4)). The

Table 5 Compressive properties and hardness of $Co_{1.5}CrFeNi_{1.5}Ti_{0.6}$ HEA

Sample	Yield strength, $\sigma_{0.2}$/MPa	Compressive strength, σ_b/MPa	Compressive strain, δ/%	Hardness, $HV_{0.5}$
T1	1183.79±90.88	1594.56±44.69	7.58±0.71	486.0±30.7
T2	1087.72±323.64	1714.86±45.79	9.14±0.60	435.7±54.4
T3	1198.71±118.66	1803.88±56.88	9.74±0.86	492.0±27.5
T4	1080.69±135.78	1810.56±28.01	11.41±0.44	442.1±27.6
T5	1179.02±66.88	1880.40±33.74	13.71±1.60	452.7±33.0
T6	1107.67±91.12	1611.94±157.40	14.27±0.71	448.8±29.1
SUS316L	302.05±2.94	−	>40	155.6±3.5
SAF2507	578.45±46.12	−	>40	246.0±4.9

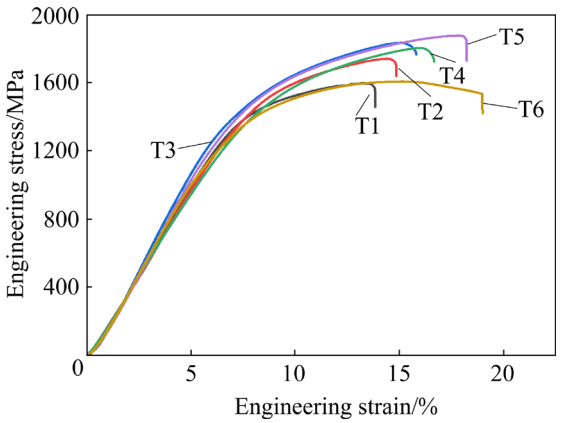

Fig. 7 Compressive engineering stress–strain curves of $Co_{1.5}CrFeNi_{1.5}Ti_{0.6}$ HEA

Cr $2p_{3/2}$ spectra exhibited three peaks at 574.3, 576.9, and 578.6 eV, corresponding to metallic Cr^0, Cr^{2+}, and Cr^{3+}, respectively, indicating the formation of Cr_2O_3 and $Cr(OH)_3$ (Figs. 10(b−b_4)). Pure Ti promoted the generation of chromium oxide [34] and a higher chromium oxide content significantly enhanced the corrosion resistance of the alloy [6]. The alloy sintered at 1050 °C exhibited higher levels of Cr_2O_3 and $Cr(OH)_3$ than other alloys, resulting in higher corrosion resistance. The deconvoluted Fe $2p_{3/2}$ spectra showed three peaks at binding energies of 711.5, 714.0, and 716.2 eV, corresponding to metallic iron Fe^0, Fe^{2+}, and Fe^{3+}, respectively (Figs. 10(c−c_4)). The Fe^{2+} species were assigned to oxides such as FeO and/or Fe_3O_4, while Fe^{3+} was associated with FeOOH and/or $Fe(OH)_3$ [25,35].

Similarly, the Ni $2p_{3/2}$ spectra (Figs. 11(a−a_4)) exhibited three fitting peaks at 855.8, 857.1, and 859.8 eV, corresponding to the metallic states Ni^0, NiO, and $Ni(OH)_2$, respectively. The low content of NiO and $Ni(OH)_2$ in all alloys was mainly due to the difficulty of Ni in forming oxides or hydroxides [8]. The Co $2p_{3/2}$ spectra featured four peaks corresponding to metallic Co^0 (778.30 eV), Co^{2+} (779.1 eV), Co^{3+} (782.0 eV), and Co^{2+}_{sat} (784.9 eV). This indicates that Co^{2+} and Co^{3+} were the main components in the Co $2p_{3/2}$ spectra (Figs. 11(b−b_4)). Additionally, the O1s spectra (Figs. 11(c−c_4)) displayed three constituent peaks corresponding to O^{2-} (530.2 eV), OH^- (531.8 eV), and H_2O (533.0 eV). These peaks represented metal oxides, metal hydroxides, and bound H_2O in the passive film [36]. Moreover, the alloy sintered at 1050 °C contained more bound H_2O in the passivation film compared with other alloys. The bound H_2O can effectively capture dissolved metal ions in the electrolyte and form a new protective film, thereby preventing further corrosion [3,35]. This process improved the corrosion resistance of the alloy.

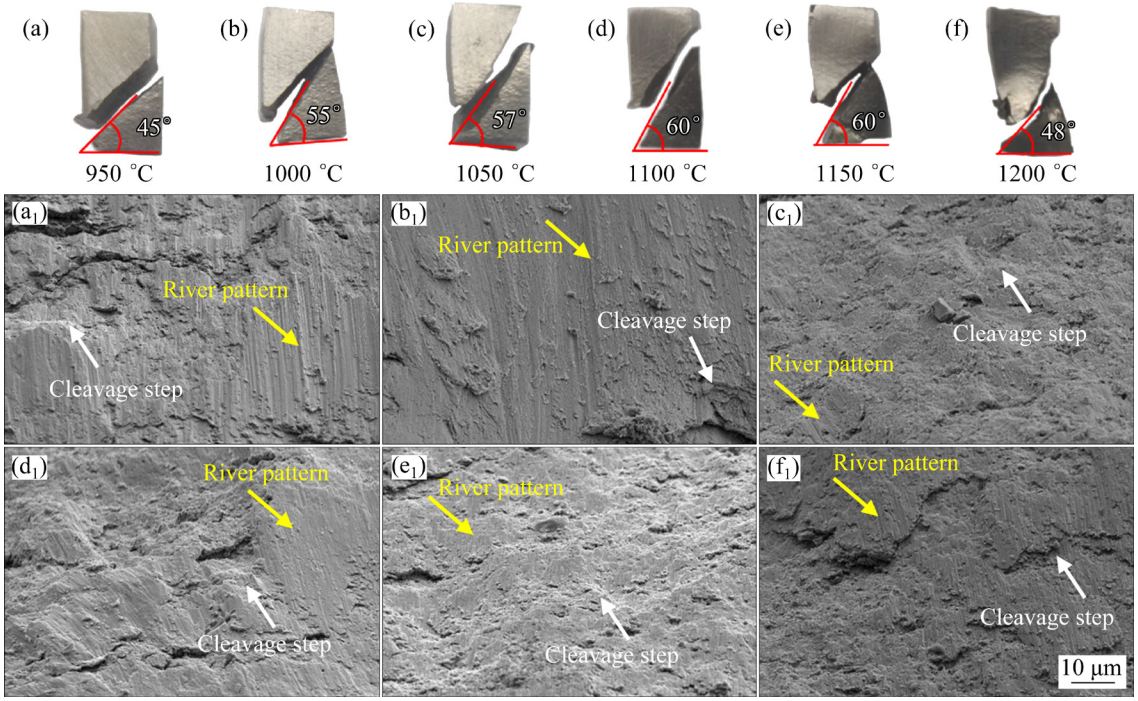

Fig. 8 Macromorphology (a−f) and micromorphology (a_1−f_1) of fracture for $Co_{1.5}CrFeNi_{1.5}Ti_{0.6}$ HEA: (a_1) 950 °C; (b_1) 1000 °C; (c_1) 1050 °C; (d_1) 1100 °C; (e_1) 1150 °C; (f_1) 1200 °C

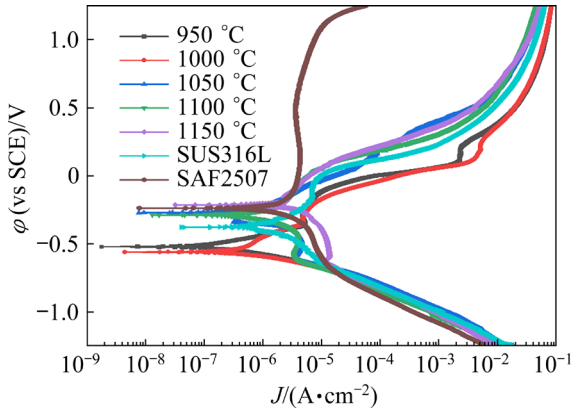

Fig. 9 Potential polarization curves of $Co_{1.5}FeCrNi_{1.5}Ti_{0.6}$ HEA, SUS316L and SAF2507 sintered at different temperatures in 3.5 wt.% NaCl solution

Table 6 Electrochemical parameters of $Co_{1.5}CrFeNi_{1.5}Ti_{0.6}$ HEA, SUS316L, and SAF2507

Sample	φ_{corr}(vs SCE)/V	J_{corr}/(A·cm^{-2})
T1	−0.522	1.47×10^{-7}
T2	−0.560	4.23×10^{-7}
T3	−0.273	7.16×10^{-7}
T4	−0.289	7.94×10^{-7}
T5	−0.214	2.22×10^{-6}
SUS316L	−0.378	8.27×10^{-7}
SAF2507	−0.238	6.41×10^{-7}

Figure 12 presents a statistical plot of the relative concentrations of cations in the passive film, as determined through XPS analysis. The passive

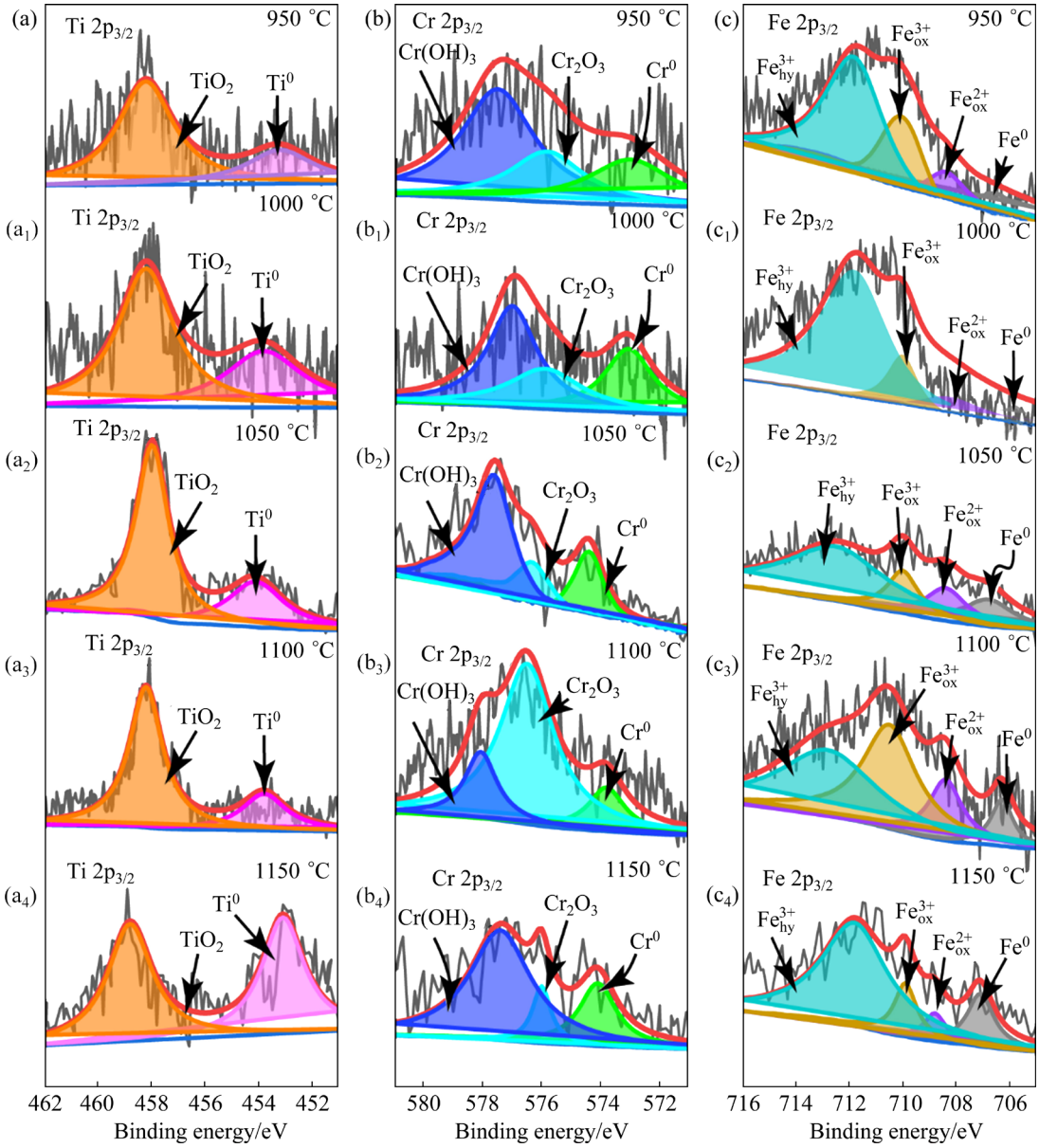

Fig. 10 XPS spectra of passivation film on $Co_{1.5}CrFeNi_{1.5}Ti_{0.6}$ HEA sintered at different temperatures in 3.5 wt.% NaCl solution: (a–a_4) Ti $2p_{3/2}$; (b–b_4) Cr $2p_{3/2}$; (c–c_4) Fe $2p_{3/2}$

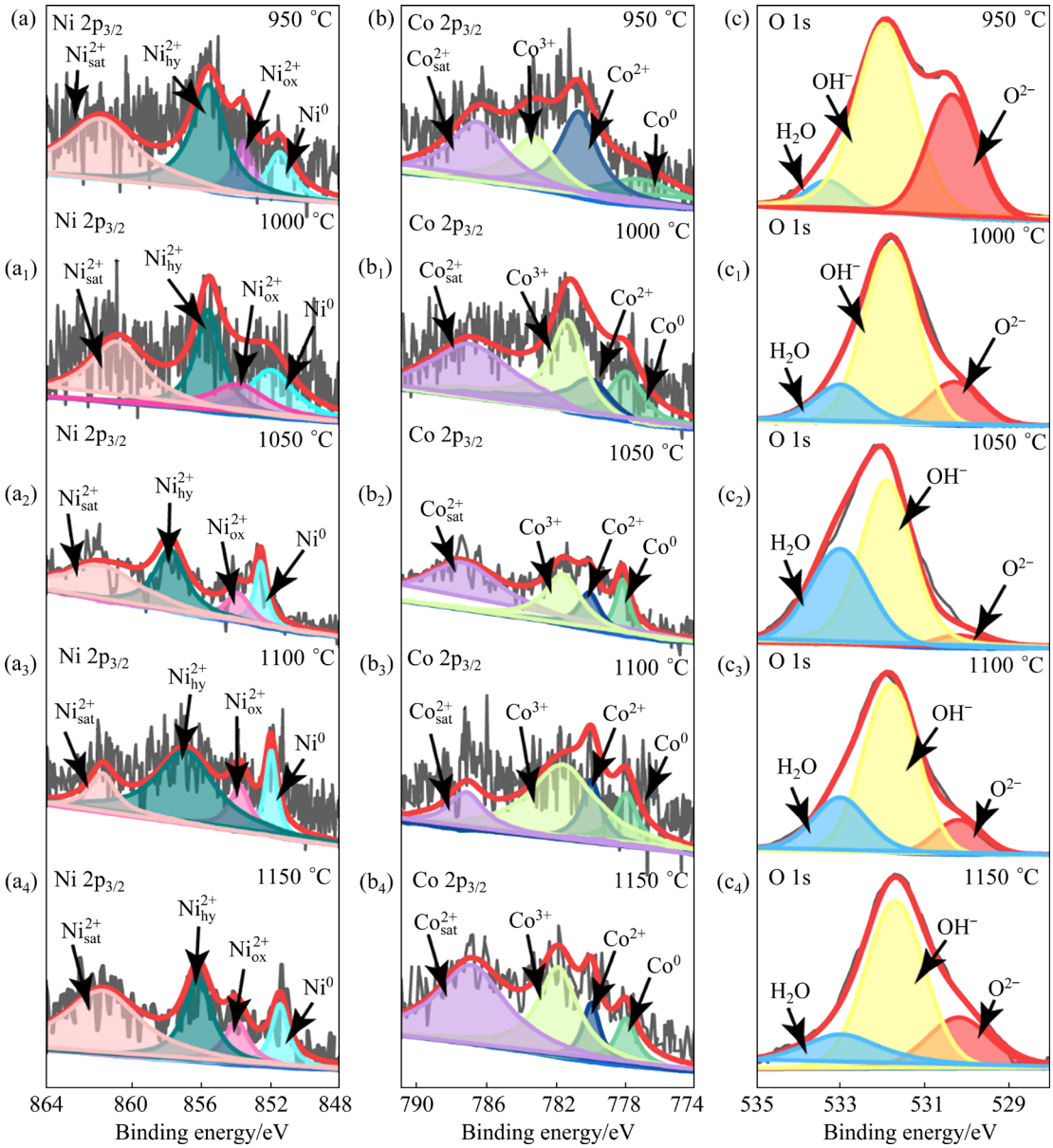

Fig. 11 XPS spectra of passivation film on $Co_{1.5}CrFeNi_{1.5}Ti_{0.6}$ HEA sintered at different temperatures in 3.5 wt.% NaCl solution: (a−a_4) Ni $2p_{3/2}$; (b−b_4) Co $2p_{3/2}$; (c−c_4) O 1s

films formed on HEAs exhibited non-uniform compositions, indicating uneven oxidation of the alloys [37]. The compositions of the passivation film on the alloys sintered at 1050, 1100, and 1150 °C exhibited a higher degree of uniformity. Conversely, the passivation films of the alloys sintered at 950 and 1000 °C had higher Fe content and lower Ti, Ni, and Cr contents. All constituent elements in each alloy were present as both oxides and unoxidized metal (M^0) species in the surface film. The metal oxides TiO_2, Cr_2O_3, Fe_2O_3, NiO, and Co_3O_4 identified in the passivation films of all samples can protect the surface in corrosive environments.

Figure 13(a) compares the J_{corr} and φ_{corr} of $Co_{1.5}CrFeNi_{1.5}Ti_{0.6}$ HEA (denoted by a grey rectangle, with an enlarged view shown in the inset) with other HEAs and conventional alloys, such as Ni alloys, stainless steels, Ti alloys, Cu alloys, and Al alloys. Both $Co_{1.5}CrFeNi_{1.5}Ti_{0.6}$ HEA and several conventional alloys were clustered in the low-J_{corr} region. However, the $Co_{1.5}CrFeNi_{1.5}Ti_{0.6}$ HEA exhibited more positive φ_{corr} value, indicating their significant potential for enhanced corrosion resistance compared with other alloys. Figure 13(b) compares the hardness and J_{corr} of $Co_{1.5}CrFeNi_{1.5}$-$Ti_{0.6}$ HEA in a 3.5 wt.% NaCl solution with those of common alloys to evaluate their anti-corrosion

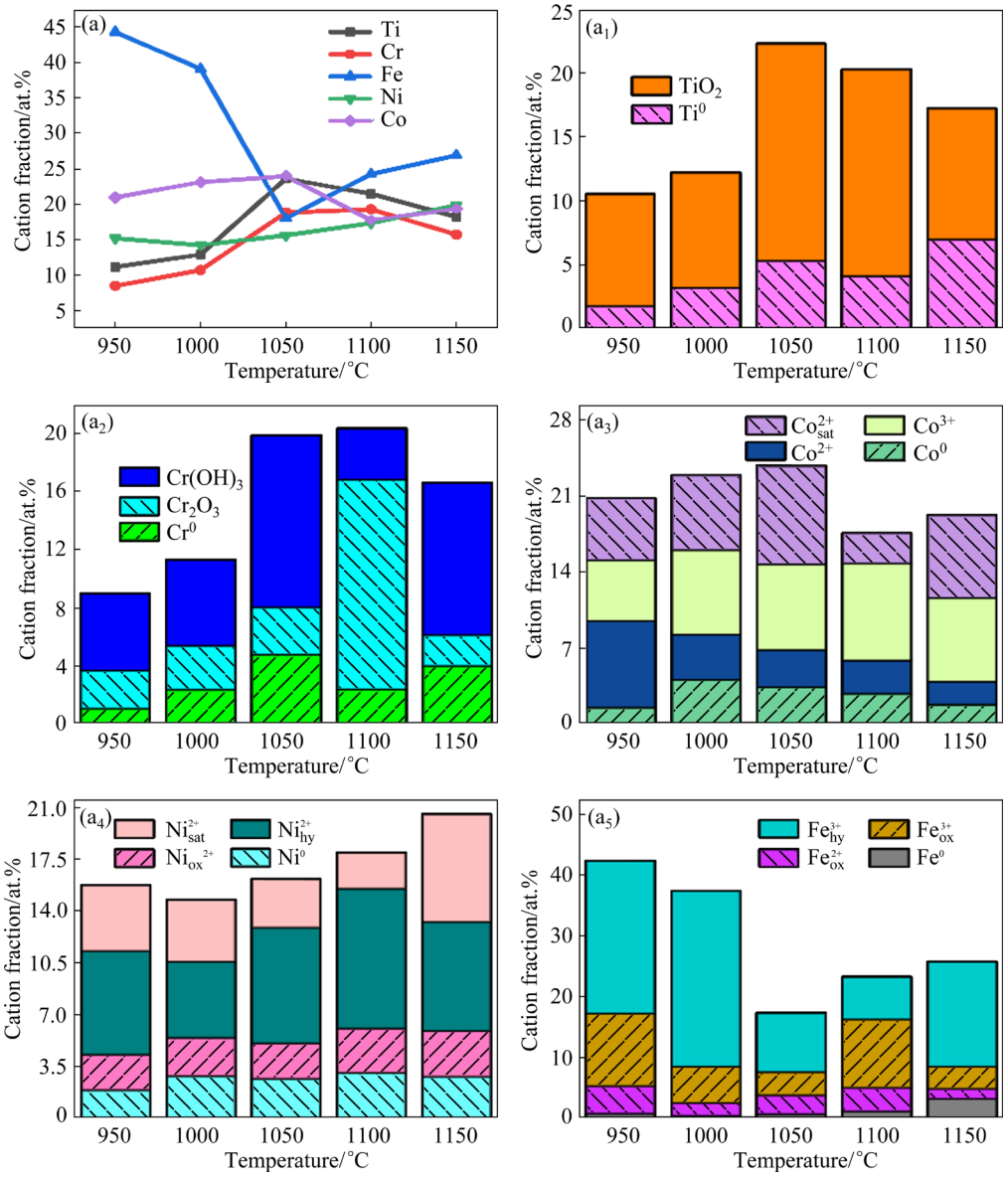

Fig. 12 (a) Composition of HEA passivation film; (a_1−a_5) Cation fractions of each component in Ti $2p_{3/2}$, Cr $2p_{3/2}$, Co $2p_{3/2}$, Ni $2p_{3/2}$, Fe $2p_{3/2}$ spectra, respectively

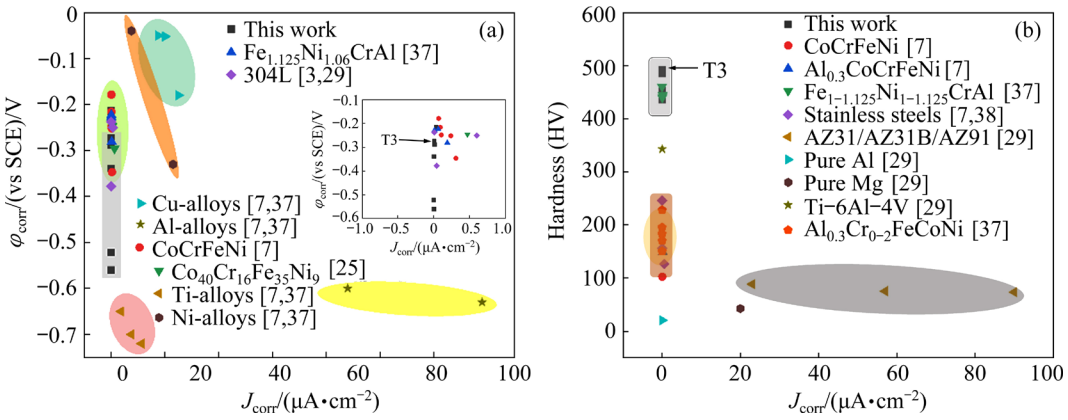

Fig. 13 (a) Comparison of φ_{corr} and J_{corr} for HEA with other reported alloys in 3.5 wt.% NaCl solution (The inset provides enlarged view of grey rectangle); (b) Comparison of hardness and J_{corr} for HEA in this study with alloys characterized by high hardness and corrosion resistance

performance and mechanical properties. The $Co_{1.5}CrFeNi_{1.5}Ti_{0.6}$ HEA featured a superior combination of high hardness and corrosion resistance than several other HEAs and conventional alloys. Moreover, the $Co_{1.5}CrFeNi_{1.5}Ti_{0.6}$ HEA sintered at 1050 °C exhibited high corrosion resistance and hardness.

4 Discussion

4.1 Microstructural evolution

The microstructural evolution process of $Co_{1.5}CrFeNi_{1.5}Ti_{0.6}$ HEA during SPS can be classified into two stages (Fig. 14). In Stage I, which occurred at different sintering temperatures, the HEA powder was subjected to high-speed impacts from high-frequency pulsed currents and discharge plasma, which purified and activated the particle surfaces. Particularly, currents of several thousand amperes can flow through the relatively small interparticle contact surfaces. This process generated a large amount of Joule heat instantaneously, which melted the tiny particles at the contact points, leading to their bonding and the formation of necks. With increasing sintering temperature, these necks expanded, leading to a significant reduction in the porosity of the HEA powder. As the pulse discharge within the powder weakened and current flowed through the conductive powder, Joule heat was generated, which significantly promoted neck growth and adhesion during the densification process.

However, the main impact of sintering temperature on the microstructure of HEAs is observed in Stage II. During this stage, as the sintering temperature increases and the heat is maintained, the neck between particles grows and bonds firmly. This process involves the diffusion and homogenization of metal atoms. Variations in the diffusion rates of metal atoms at different temperatures led to the formation of distinct microstructures, which are further influenced by the significant hysteresis diffusion effect in HEAs. At sintering temperature of 950 or 1000 °C, atom diffusion and neck growth occur. Upon cooling after the retention of these temperatures, the material gradually forms the FCC matrix phase. Subsequently, coarse dendritic structures of *R* and *ε* phases precipitate in the FCC matrix owing to the low mixing enthalpy of Ni and Ti (−35 kJ/mol), which is the lowest among the Cr, Fe, Ni, Ti, and Co elements. As the temperature decreases, Ni and Ti undergo an ordered transition to form the *R* and *ε* phases [11]. With the precipitation of large amounts of *R* and *ε* phase precipitates, the relative concentration of Fe and Cr atoms in localized regions

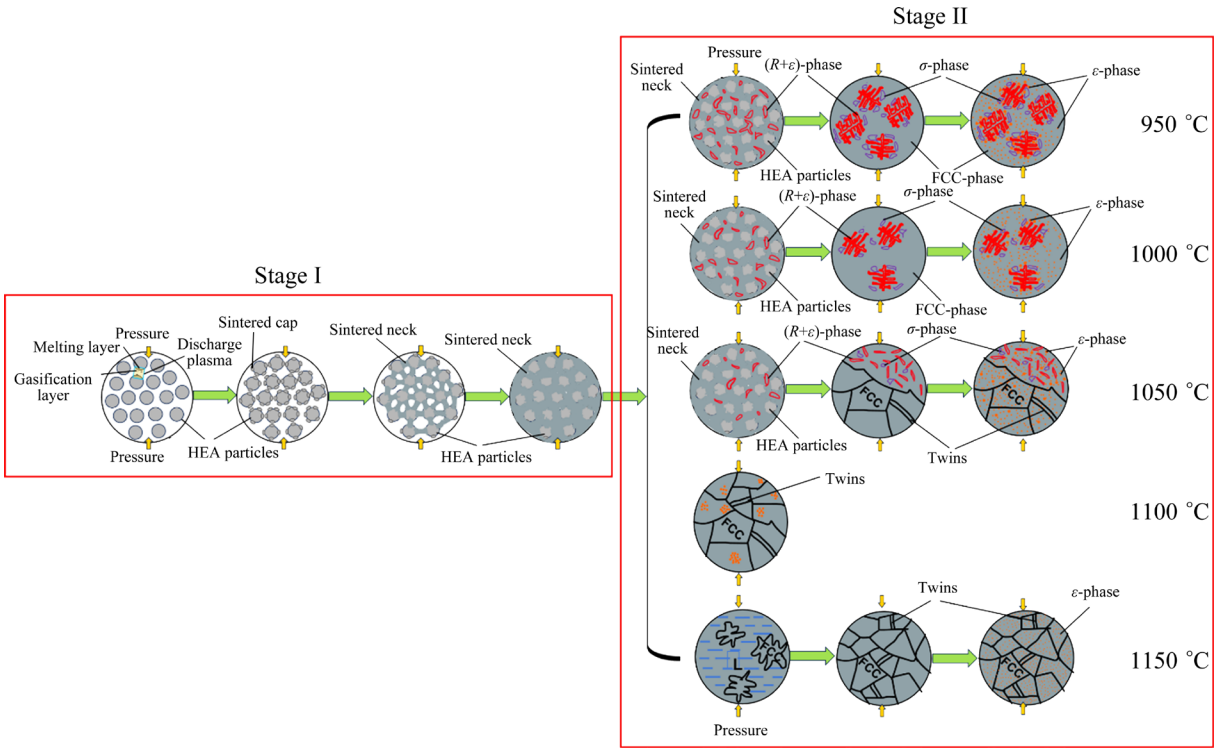

Fig. 14 Microstructural evolution of $Co_{1.5}CrFeNi_{1.5}Ti_{0.6}$ HEA prepared at different sintering temperatures during SPS

increases, leading to the formation of a Fe- and Cr-rich disordered solid solution (σ phase). Consequently, a small number of σ-phase diffraction peaks is detected in HEAs sintered at 950 and 1000 °C (Fig. 1(b)). As the temperature further decreases, atom diffusion and homogenization are hindered, leading to the precipitation of Ni and Ti as ε-phases in small quantities. As the temperature continuously decreases, HEAs lack sufficient energy to overcome the potential barrier for atomic migration, resulting in the formation of nanoparticles from a limited number of Ti and Ni atoms. Similar results have been reported in the literature [11,18,29,39].

At a sintering temperature of 1050 °C, the FCC matrix phase initially forms as the temperature decreases. Owing to the relatively high temperature, the FCC matrix can dissolve a large amount of Ni and Ti atoms, with only a small fraction of these atoms remaining in the matrix. These remaining Ni and Ti atoms aggregate to form small quantities of R and ε phases. Additionally, a minimal amount of σ phase precipitates around the R and ε phases. The sintered body exhibits a non-uniform distribution of Ni and Ti atoms owing to the relatively low diffusion rate of metal atoms and the delayed diffusion effect in HEAs. Consequently, fine equiaxed crystals are formed in certain regions. A further decrease in the temperature hinders the diffusion and homogenization of atoms, causing Ni and Ti to precipitate as ε-phases in the FCC matrix. Therefore, the alloy microstructure consists of fine equiaxed crystals and short rod-like dendrites (Figs. 2(c, c_1)). At a sintering temperature of 1100 °C, the metal atoms exhibit sufficient diffusion and homogenization. As the temperature decreases, the FCC matrix phase is formed, which can dissolve a large amount of Ni and Ti atoms. However, owing to the high Ti and Ni content, some regions in the matrix exhibit insufficient diffusion, enabling these small areas to form R- and ε-phase nanoparticles. After rapid cooling, the alloy solidifies into a simple FCC solid solution structure with fine equiaxial grains. At a sintering temperature of 1150 °C, some areas of the alloy partially melt, similar to the as-cast state. During this process, the FCC matrix phase initially forms, followed by the precipitation of the ε phase, which is uniformly distributed in the FCC matrix.

4.2 Strengthening mechanism analysis

According to the analysis in Section 3.3, the $Co_{1.5}CrFeNi_{1.5}Ti_{0.6}$ HEA sintered at 1050 °C exhibited the highest comprehensive mechanical properties. The strengthening mechanisms of HEAs can be attributed to solid-solution strengthening ($\Delta\sigma_{SS}$), dislocation strengthening ($\Delta\sigma_{Dis}$), grain boundary strengthening ($\Delta\sigma_{GB}$), twin grain boundary strengthening ($\Delta\sigma_{TB}$), and precipitation strengthening ($\Delta\sigma_{P}$). The contributions of these mechanisms to yield strength ($\sigma_{0.2}$) are expressed as follows:

$$\sigma_{0.2}=\sigma_0+\Delta\sigma_{SS}+\Delta\sigma_{Dis}+\Delta\sigma_{GB}+\Delta\sigma_{TB}+\Delta\sigma_{P} \quad (1)$$

where σ_0 represents the lattice friction strength. According to existing reports [40], the σ_0 value is 165 MPa.

4.2.1 Solid-solution strengthening

The XRD and SEM results revealed that Ti atoms were fully dissolved in the FCC matrix of HEAs, which replaced the small atoms present in the original FCC matrix phase. Consequently, lattice distortion increased (Fig. 5(b)), which hindered dislocation motion and led to solid-solution strengthening [18,39,41,42]. Because the $Co_{1.5}CrFeNi_{1.5}Ti_{0.6}$ HEA can be regarded as a matrix with Ti solute in a CoCrFeNi solvent, the standard model for substitutional solid-solution strengthening based on dislocation-solute elasticity can be used to assess the efficiency of Ti-induced solution strengthening [12,43].

$$\Delta\sigma_{SS}=M\frac{G\varepsilon_S^{3/2}\cdot c^{1/2}}{700} \quad (2)$$

where G represents the shear modulus of Ti (~42 GPa), c denotes the total molar fraction of Ti in the FCC matrix (c=10.8 at.%), and M=3.06 represents the Taylor factor [44]. The interaction parameter ε_S is expressed as follows:

$$\varepsilon_S=\left|\frac{\varepsilon_G}{1+0.5\varepsilon_G}-3\varepsilon_a\right| \quad (3)$$

This formula combines the effects of elastic and atomic mismatches, denoted as ε_G and ε_a, respectively, which are defined as follows:

$$\varepsilon_G=\frac{1}{G}\frac{\partial G}{\partial c} \quad (4)$$

$$\varepsilon_a=\frac{1}{a}\frac{\partial_a}{\partial_c} \quad (5)$$

where a represents the lattice constant of the CoCrFeNi HEA matrix (a=0.3546 nm) [43]. ε_a can be determined from the lattice constants of the CoCrFeNi matrix and $Co_{1.5}CrFeNi_{1.5}Ti_{0.6}$ (with a= 0.3585 nm). Generally, ε_G is considered negligible compared with ε_a [45]. Accordingly, the strength enhancement caused by solid-solution strengthening in the $Co_{1.5}CrFeNi_{1.5}Ti_{0.6}$ is calculated to be ~10.2 MPa.

4.2.2 Dislocation strengthening

Generally, intense deformation during MA generates numerous defects such as dislocations, twins, and other defects, which are retained after sintering. The dislocation density of $Co_{1.5}CrFeNi_{1.5}Ti_{0.6}$ HEA can be estimated using the following equation [43]:

$$\rho=\frac{2\mathrm{KAM}_{\mathrm{avg.}}}{\mu b} \tag{6}$$

where μ represents the step size (μ=0.12 μm), b denotes the magnitude of Burgers vector ($b=\sqrt{2}/2a$), and a indicates the lattice constant of the FCC structure. For the $Co_{1.5}CrFeNi_{1.5}Ti_{0.6}$ HEA, b is ~0.254 nm. The average kernel average misorientation ($KAM_{avg.}$) (measured in degrees and converted to radians) is calculated using the following equation:

$$\mathrm{KAM}_{\mathrm{av}}=\exp\left[\frac{1}{N}\sum_{1}^{i}\ln \mathrm{KAM}_{\mathrm{L},i}\right] \tag{7}$$

where $KAM_{L,i}$ represents the local KAM value at point i, and N represents the number of points in the test area. Both $KAM_{L,i}$ and N are obtained from EBSD-KAM data shown in Fig. 6. The dislocation density ρ of $Co_{1.5}CrFeNi_{1.5}Ti_{0.6}$ HEA is calculated to be 1.18×10^{14} m^{-2}. The dislocation strengthening, $\Delta\sigma_{Dis}$, can be described using the Bailey–Hirsch formula:

$$\Delta\sigma_{\mathrm{Dis}}=M\alpha Gb\rho^{1/2} \tag{8}$$

where M represents the mean orientation factor (M= 3.06), α=0.2 is a constant for FCC metals [46], and G indicates the shear modulus (~74 GPa) [12]. Dislocation strengthening contributes ~125.0 MPa to the overall strength.

4.2.3 Grain boundary strengthening

The fine grain strengthening ($\Delta\sigma_{GB}$) can be describe using the Hall−Petch equation [47].

$$\Delta\sigma_{\mathrm{GB}}=K^{\mathrm{HP}(nc)}d^{-1/2} \tag{9}$$

where $K^{HP(nc)}$ is the strengthening coefficient, and d denotes the average grain diameter (d=0.87 μm). The Hall−Petch coefficient ($K^{HP(nc)}$) typically decreases significantly with decreasing grain size, particularly as the grain size approaches the nanocrystalline range [48]. Literature indicates that the $K^{HP(nc)}$ of coarse-grained HEAs are generally similar to that of iron-based materials [12,49,50]. The $K^{HP(nc)}$ of pure iron decreases from 600 to 350 MPa·μm$^{1/2}$ as the grain size decreases from coarse to nanocrystalline [51,52]. In this study, a $K^{HP(nc)}$ value of 350 MPa·μm$^{1/2}$ was selected. Consequently, $\Delta\sigma_{GB}$ contributed ~375.2 MPa to the yield strength.

4.2.4 Twin grain boundary strengthening

The effect of twin grain boundary strengthening is similar to that of grain boundary strengthening. The twin grain boundary strengthening ($\Delta\sigma_{TB}$) is calculated using the following equation [53]:

$$\Delta\sigma_{\mathrm{TB}}=V_{\mathrm{T}}K^{\mathrm{TB}}\lambda^{-1/2} \tag{10}$$

where K^{TB} represents a constant approximately equal to $K^{HP(nc)}$, λ represents the average thickness of the twin layers (λ=0.091 μm, which is extracted from Fig. 6(c) and estimated using ImageJ software), and V_T denotes the volume fraction of twins (V_T=16.3%). The calculated twin grain boundary strengthening $\Delta\sigma_{TB}$ of $Co_{1.5}CrFeNi_{1.5}Ti_{0.6}$ HEA is ~189.1 MPa.

4.2.5 Precipitation strengthening

The precipitation strengthening of the ε-phase nanoparticles can be described through the Orowan mechanism [12,32]. Orowan strengthening is particularly significant in alloys with particle sizes below 1 μm [54]. In this study, the ε-phase particles were below 1 μm. Consequently, the contribution of these particles to the increase in yield strength can be estimated using the following formula [43,45]:

$$\Delta\sigma_{\mathrm{P}}=0.81M\frac{\gamma_{\mathrm{APB}}}{2b}\left(\frac{3\pi f}{8}\right)^{1/2} \tag{11}$$

where M represents the Taylor factor for the FCC matrix (M=3.06), γ_{APB} denote the anti-phase boundary energy of the nanoparticles (~0.12 J/m^2) [52]. The volume fraction f of the nanoparticles calculated from (Fig. 4(c)) was ~35.7%. Thus, $\Delta\sigma_P$ contributed ~357.4 MPa to the yield strength.

In summary, the calculated yield strength $\sigma_{0.2}$ of the $Co_{1.5}CrFeNi_{1.5}Ti_{0.6}$ HEA was ~1221.9 MPa, which closely matches the experimental value of

1198.7 MPa. These results indicate that precipitation strengthening and grain boundary strengthening were the main mechanisms contributing to material strength.

Figure 15 shows the compressive strength and strain of some representative HEAs. Compared with other HEAs, the $Co_{1.5}CrFeNi_{1.5}Ti_{0.6}$ HEA exhibited higher comprehensive properties. The excellent strength and plasticity of the alloy can be attributed to the plastic characteristics of the FCC phase and the spatial distribution of nanoscale and micron-sized reinforcing precipitates [29,56].

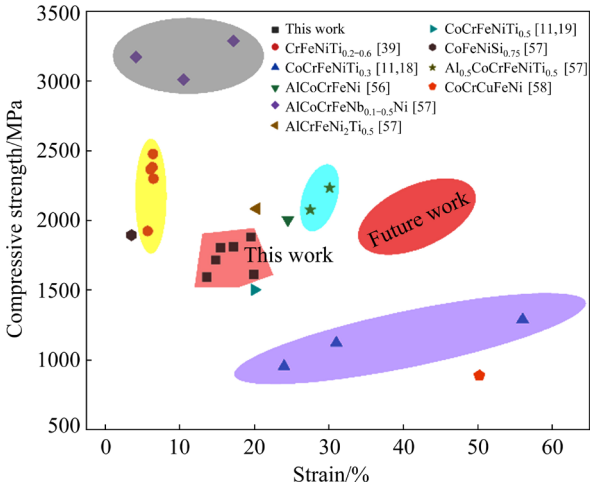

Fig. 15 Comparison of compressive strength of HEA in this study with values reported in literature

4.3 Electrochemical corrosion properties

The $Co_{1.5}CrFeNi_{1.5}Ti_{0.6}$ HEA sintered at 1050 °C exhibited excellent corrosion resistance in a 3.5 wt.% NaCl solution compared with other HEAs (Section 3.4). This superior performance can be attributed to the properties of the passive film and the microstructure.

Polarization curve analysis revealed that HEAs with homogeneous composition of passivation films exhibited superior corrosion resistance owing to the high Cr^{3+} and TiO_2 contents and a low Fe content in these films. This finding further confirmed the selective dissolution of the alloy surface during the corrosion of HEAs [29,37]. The uniformity and composition of the passivation film were key factors influencing the corrosion properties of HEAs. Compared with other samples, the sample sintered at 1050 °C contained higher levels of Cr^{3+}, TiO_2, and bound H_2O in the passive film. Studies have shown that Cr^{3+} significantly enhances the compactness of the passive film [34,35], with higher Cr concentrations leading to enhanced corrosion resistance. Additionally, TiO_2 particles in the film filled the voids, thereby increasing the density of the film layer and significantly improving its corrosion resistance [29,35]. This finding indicates that the high levels of Cr^{3+} and TiO_2 in the alloy sintered at 1050 °C significantly enhanced its corrosion resistance. Moreover, bound H_2O at the interface can absorb metal ions and form a protective film, further preventing the corrosion of the alloy. Notably, the alloy sintered at 1050 °C exhibited the highest content of bound H_2O in the passivation film, which correlated with its superior corrosion resistance [3,35]. Furthermore, statistical analysis indicated that the passivation film composition of this alloy exhibited higher uniformity, contributing to its enhanced corrosion resistance.

The microstructural analysis (Fig. 2) revealed that at lower sintering temperatures, the presence of coarse dendritic crystals and a small amount of σ-phase in HEAs led to potential differences between the R-phase, ε-phase, σ-phase, and FCC matrix phase. This variation caused significant microcell corrosion effects between the phases, thereby reducing the corrosion resistance of HEAs. As the sintering temperature increased, the microstructure of HEAs changed from coarse dendrites to fine equiaxial crystals, which reduced elemental segregation. This change mitigated the microcell corrosion effect and improved the corrosion resistance of HEAs. The alloy sintered at 1050 °C contained numerous microscale R and ε phases, and their small size further reduced the microcell corrosion effects with the FCC matrix phase. Additionally, Ti exhibited strong resistance to brine (Cl^-) corrosion. Therefore, the incorporation of Ti into the alloy can effectively mitigate the reduction in corrosion resistance associated with the fine R phases [25,35,37].

5 Conclusions

(1) The diffusion rates, homogenization, and sluggish diffusion effects of metal atoms influenced the microstructure and phase composition of $Co_{1.5}CrFeNi_{1.5}Ti_{0.6}$ HEA. At sintering temperatures below 1050 °C, HEAs mainly featured the FCC matrix phase, ε-phase, R-phase and σ-phase, and exhibited a microstructure characterized by

dendritic crystals. At 1050 °C, the microstructure consisted of short rod-like dendrites and fine equiaxed crystals. However, HEAs sintered above 1100 °C contained only fine equiaxed crystals.

(2) The plasticity of $Co_{1.5}CrFeNi_{1.5}Ti_{0.6}$ HEA gradually improved with increasing sintering temperature. The alloy sintered at 1050 °C achieved an optimal balance between hardness, plasticity, and compressive strength. The strengthening mechanisms mainly included solid-solution strengthening, dislo-cation strengthening, grain boundary strengthening, twin grain boundary strengthening, and precipitation strengthening. Precipitation strengthening and grain boundary strengthening were the main contributors to the improved yield strength of HEAs.

(3) The $Co_{1.5}CrFeNi_{1.5}Ti_{0.6}$ HEA exhibited superior corrosion resistance. The passivation films of these HEAs comprised all constituent elements in the form of oxides, hydroxides, and unoxidized metals. The alloy sintered at 1050 °C achieved the highest levels of TiO_2, Cr_2O_3, and bound H_2O in the passivation film, resulting in the highest corrosion resistance.

CRediT authorship contribution statement

Chao WANG: Conceptualization; Investigation, Data curation, Formal analysis, Methodology, Visualization, Writing − Original draft, Writing − Review and editing, Preparation; **Wei-zheng AN**, **Qiang MA** and **Xiang WANG:** Resources, Project administration, Funding acquisition, Writing − Review and editing; **Jia-xin LI** and **Zhao-yang LIANG:** Writing − Review and editing, Supervision; **Qi-dong NIE:** Investigation, Methodology.

Declaration of competing interest

The authors declare that they have no known competing financial interests or personal relationships that could have appeared to influence the work reported in this paper.

Acknowledgments

This work is supported by Special Fund for the Development of 1500-Meter Subsea Christmas Trees and Control Systems.

References

[1] LI Zhi-ming, PRADEEP K G, DENG Yun, RAABE D, TASAN C C. Metastable high-entropy dual-phase alloys overcome the strength−ductility trade-off [J]. Nature, 2016, 534: 227−230.

[2] HAO Xiu-hong, ZHEN Jin-ming, ZHAO Xiao-ming, MA Jie, CHEN Hui, GUO Shao-yun, WANG Chang-gang, WANG Chang-zheng. Effect of Sn addition on the tribological behaviors of CoCrFeNi high entropy alloys [J]. Journal of Alloys and Compounds, 2022, 909: 164657.

[3] LU Qing-qing, CHEN Xiao-hong, TIAN Wei, WANG Hao, LIU Ping, ZHOU Hong-lei, FU Shao-li, GAO Yu-hang, WAN Mao-yuan, WANG Xin-jiao. Corrosion behavior of a non-equiatomic CoCrFeNiTi high-entropy alloy: A comparison with 304 stainless steel in simulated body fluids [J]. Journal of Alloys and Compounds, 2022, 897: 163036.

[4] ZHANG Xian-man, CHEN Zai-yu, LUO Hong-feng, ZHOU Teng, ZHAO Yu-liang, LING Zi-cheng. Corrosion resistances of metallic materials in environments containing chloride ions: A review [J]. Transactions of Nonferrous Metals Society of China, 2022, 32: 377−410.

[5] GELCHINSKI B R, BALYAKIN I A, YURYEV A A, REMPEL A A. High entropy alloys: Properties and prospects of application as protective coatings [J]. Russian Chemical Reviews, 2022, 91(6): RCR5023.

[6] LUO Hong, LI Zhi-ming, MINGERS A M, RAABE D. Corrosion behavior of an equiatomic CoCrFeMnNi high-entropy alloy compared with 304 stainless steel in sulfuric acid solution [J]. Corrosion Science, 2018, 134: 131−139.

[7] SHI Yao-hui, YANG Bin, XIE Xie, BRECHTL J, DAHMEN K A, LIAW P K. Corrosion of Al_xCoCrFeNi high-entropy alloys: Al-content and potential scan-rate dependent pitting behavior [J]. Corrosion Science, 2017, 119: 33−45.

[8] SHUANG S, DING Z Y, CHUNG D, SHI S Q, YANG Y. Corrosion resistant nanostructured eutectic high entropy alloy [J]. Corrosion Science, 2020, 164: 108315.

[9] SUN Yuan-wei, WANG Zi-yi, ZHAO Xiang-jin, LIU Zhong-li, CAO Fu-hua. Effects of Sc addition on microstructure, phase evolution and mechanical properties of $Al_{0.2}$CoCrFeNi high-entropy alloys [J]. Transactions of Nonferrous Metals Society of China, 2023, 33: 3756−3769.

[10] DIAO Hui-diao, FENG Rui, DAHMEN K A, LIAW P K. Fundamental deformation behavior in high-entropy alloys: an overview [J]. Current Opinion in Solid State & Materials Science, 2017, 21(5): 252−266.

[11] SHUN Tao-tsung, CHANG Liang-yi, SHIU Ming-hua. Microstructures and mechanical properties of multiprincipal component CoCrFeNiTi_x alloys [J]. Materials Science and Engineering: A, 2012, 556: 170−174.

[12] HE J Y, LIU W H, WANG H, WU Y, LIU X J, NIEH T G, LU Z P. Effects of Al addition on structural evolution and tensile properties of the FeCoNiCrMn high entropy alloy system [J]. Acta Materialia, 2014, 62: 105−113.

[13] ZHU Ze-lin, NGUYEN Q B, NG F L, AN Xiang-hai, LIAO Xiao-zhou, LIAW P K, NAI S M L, WEI Jun. Hierarchical microstructure and strengthening mechanisms of a CoCrFeNiMn high entropy alloy additively manufactured by selective laser melting [J]. Scripta Materialia, 2018, 154: 20−24.

[14] FU Zhi-qiang, CHEN Wei-ping, XIAO Hui-ning, ZHOU Li-wei, ZHU Dao-ben, YANG Shao-feng. Fabrication and properties of nanocrystalline $Co_{0.5}$FeNiCr$Ti_{0.5}$ high entropy alloy by MA-SPS technique [J]. Materials & Design, 2013, 44: 535−539.

[15] CHEN Si-jing, OH H S, GLUDOVATZ B, KIM S J, PARK E S, ZHANG Ze, RITCHIE R O, YU Qian. Real-time observations of TRIP-induced ultrahigh strain hardening in a dual-phase CrMnFeCoNi high-entropy alloy [J]. Nature

Communications, 2020, 11(1): 826.

[16] YOOSEFAN F, ASHRAFI A, VAGHEFI S M M. Enhanced mechanical and corrosion properties of cold-rolled CoCrFeMoNi high-entropy alloy, as a proposed material for vascular stents [J]. Materials Characterization, 2023, 205: 113343.

[17] WU Peng-fei, GAN Ke-fu, YAN Ding-shun, FU Zheng-hong, LI Zhi-ming. A non-equiatomic FeNiCoCr high-entropy alloy with excellent anti-corrosion performance and strength−ductility synergy [J]. Corrosion Science, 2021, 183: 109341.

[18] HUANG Wei-jue, SHUN Tao-tsung, CHIANG Cheng-ju. Effects of reducing Co content on microstructure and mechanical properties of $Co_xCrFeNiTi_{0.3}$ high-entropy alloys [J]. Materials Chemistry and Physics, 2018, 210: 170−175.

[19] WANG Xin-yang, LIU Qian, HUANG Yan-bin, XIE Lu, XU Quan, ZHAO Tian-xiang. Effect of Ti content on the microstructure and corrosion resistance of $CoCrFeNiTi_x$ high entropy alloys prepared by laser cladding [J]. Materials, 2020, 13(10): 2209.

[20] ASL M S, NAMINI A S, MOTALLEBZADEH A, AZADBEH M. Effects of sintering temperature on microstructure and mechanical properties of spark plasma sintered titanium [J]. Materials Chemistry and Physics, 2018, 203: 266−273.

[21] ZADRA M, CASARI F, GIRARDINI L, MOLINARI A. Microstructure and mechanical properties of cp-titanium produced by spark plasma sintering [J]. Powder Metallurgy, 2008, 51: 59−65.

[22] ZHENG Qi-feng, LU Wen-jian, HAN Da-wei, LI Tian-run, GUO Hui, QIU Ke-qiang, YANG Bai-jun, WANG Jian-qiang. Effect of Al content on microstructure, mechanical and corrosion properties of $(Fe_{33}Cr_{36}Ni_{15}Co_{15}Ti_1)100_{1-x}Al_x$ high-entropy alloys [J]. Advanced Engineering Materials, 2023, 25: 2301013.

[23] WANG Li, DONG Chao-fang, YAO Ji-zheng, DAI Zong-biao, MAN Cheng, YIN Yu-peng, XIAO Kui, LI Xiao-gang. The effect of η-Ni_3Ti precipitates and reversed austenite on the passive film stability of nickel-rich Custom 465 steel [J]. Corrosion Science, 2019, 154: 178−190.

[24] ZEISL S, LANDEFELD A, van STEENBERGE N, CHANG Y, SCHNITZER R. The role of alloying elements in NiAl and Ni_3Ti strengthened Co-free maraging steels [J]. Materials Science and Engineering: A, 2022, 861: 144313.

[25] CHEN Xiao-hong, LU Qing-qing, GAO Yu-hang, TIAN Wei, WANG Hao, ZHOU Hong-lei, FU Shao-li, LIU Ping, WANG Xin-jiao, JIANG Tao, WAN Mao-yuan. Bidirectional improvement of strength and ductility of CoCrFeNiTi ($Co_{40}Cr_{16}Fe_{35}Ni_8Ti_1$) high-entropy alloys suitable for coronary stents [J]. Journal of Materials Research and Technology, 2022, 18: 1934−1946.

[26] JIANG Li, LU Yi-ping, DONG Yong, WANG Tong-min, CAO Zhi-qiang, LI Ting-ju. Annealing effects on the microstructure and properties of bulk high-entropy $CoCrFeNiTi_{0.5}$ alloy casting ingot [J]. Intermetallics, 2014, 44: 37−43.

[27] ZHANG Shi-yi, HAN Bin, LI Mei-yan, ZHANG Qi, HU Chun-yang, NIU Sheng-yuan, LI Zhao-hui, WANG Yong. Investigation on solid particles erosion resistance of laser cladded CoCrFeNiTi high entropy alloy coating [J]. Intermetallics, 2021, 131: 107111.

[28] XIANG Hai-yan, ZHENG Yue-shao, SUN Yue, GUO Ting-ting, ZHANG Pei, LI Wei, KONG Shi-wei, OUZOUNIAN M, CHEN Hong, LI Hui-min, HU T S, YU Gang, FENG Ye-xin, LIU Song. Bimetallic and postsynthetically alloyed PtCu nanostructures with tunable reactivity for the methanol oxidation reaction [J]. Nanoscale Advances, 2020, 2(4): 1603−1612.

[29] QIU Y, THOMAS S, FABIJANIC D, BARLOW A J, FRASER H L, BIRBILIS N. Microstructural evolution, electrochemical and corrosion properties of $Al_xCoCrFeNiTi_y$ high entropy alloys [J]. Materials & Design, 2019, 170: 107698.

[30] RAFAILOVIĆ L D, GAMMER C, EBNER C, RENTENBERGER C, JOVANOVIĆ A Z, PAŠTI I A, SKORODUMOVA N V, H. PETER KARNTHALER H P. High density of genuine growth twins in electrodeposited aluminum [J]. Science Advances, 2019, 5(10): eaax3894.

[31] WU Y H, CHEN J S, JI J Y, ZHANG Y Z, WANG Q Z, XIONG K. Structural stability, elasticity, thermodynamics, and electronic structures of $L1_2$-type Ni_3X (X = Al, Ti, V, Nb) phases under external pressure condition [J]. Journal of Molecular Modeling, 2022, 28(1): 26.

[32] ZHANG Han-wen, LIU Pei-zhi, HOU Jin-xiong, QIAO Jun-wei, WU Yu-cheng. Prediction of strength and ductility in partially recrystallized $CoCrFeNiTi_{0.2}$ high-entropy alloy [J]. Entropy, 2019, 21(4): 389.

[33] QIN Hai-xu, QU Wan-bo, ZHANG Yang, ZHANG Yong-sheng, LIU Zi-hang, ZHANG Qian, WU Hai-jun, CAI Wei, SUI Jie-he. Nanotwins strengthening high thermoelectric performance bismuth antimony telluride alloys [J]. Advanced Science, 2022, 9(14): 2200432.

[34] KOCIJAN A, DONIK Č, JENKO M. Electrochemical and XPS studies of the passive film formed on stainless steels in borate buffer and chloride solutions [J]. Corrosion Science, 2007, 49(5): 2083−2098.

[35] LU Ke-jie, LI Jia-hao, WANG You-fan, MA Xin-kai. Excellent strength-ductility synergy and corrosion resistance in a metastable high entropy alloy via heterogeneous structure design [J]. Journal of Alloys and Compounds, 2023, 941: 168979.

[36] HAN Zhen-hua, REN Wei-ning, YANG Jun, TIAN A-li, DU Yu-zhou, LIU Gang, WEI Ran, ZHANG Guo-jun, CHEN Yuan-qing. The corrosion behavior of ultra-fine grained CoNiFeCrMn high-entropy alloys [J]. Journal of Alloys and Compounds, 2020, 816: 152583.

[37] CUI Pu-chang, BAO Zhi-jia, LIU Yong, ZHOU Fei, LAI Zhong-hong, ZHOU Ying, ZHU Jing-chuan. Corrosion behavior and mechanism of dual phase $Fe_{1.125}Ni_{1.06}CrAl$ high entropy alloy [J]. Corrosion Science, 2022, 201: 110276.

[38] NENE S S, FRANK M, LIU K, SINHA S, MISHRA R S, MCWILLIAMS B A, CHO K C. Corrosion-resistant high entropy alloy with high strength and ductility [J]. Scripta Materialia, 2019, 166: 168−172.

[39] GAO Shuo, KONG Teng, ZHANG Man, CHEN Xiao, SUI Yan-wen, REN Yao-jian, QI Ji-qiu, WEI Fu-xiang, HE Ye-zeng, MENG Qing-kun, SUN Zhi. Effects of titanium addition on microstructure and mechanical properties of $CrFeNiTi_x$ (x=0.2~0.6) compositionally complex alloys [J]. Journal of Materials Research, 2019, 34(5): 819−828.

[40] LIN Kuan-hao, TSENG Chieh-min, CHUEH Chu-chun, CHANG Shou-yi, LO Yu-chieh, WANG Chun-chieh, LIN Su-jien, YEH Jien-wei. Different lattice distortion effects on the tensile properties of Ni−W dilute solutions and CrFeNi and CoCrFeMnNi concentrated solutions [J]. Acta Materialia, 2021, 221: 117399.

[41] ZHANG Y, ZHOU Y J, LIN J P, CHEN G L, LIAW P K. Solid-solution phase formation rules for multi-component alloys [J]. Advanced Engineering Materials, 2008, 10:

534−538.
[42] HE Yi, LI Wei-guo, PI Wen-li, YANG Meng-qing, DONG Pan, ZHANG Zhi-qing. Physics-based model to predict yield strength of single-phase FCC high-entropy alloys over wide temperature range [J]. Transactions of Nonferrous Metals Society of China, 2023, 33:3770−3782.
[43] LI Jing-jing, OUYANG Di, WANG Qi-hang, TENG Qing, CAI Chao, WEI Qing-song. Achieving superior tensile strength of $CoCrFeNiTi_{0.3}$ high-entropy alloy via in-situ laser powder bed fusion of CoCrFeNi and Ti [J]. Materials Science and Engineering: A, 2023, 886: 145649.
[44] TAYLOR G I. The mechanism of plastic deformation of crystal. Part I: Theoretical [J]. Proceedings of the Royal Society A, 1934, 145(855): 362−387.
[45] HE J Y, WANG H, HUANG H L, XU X D, CHEN M W, WU Y, LIU X J, NIEH T G, AN K, LU Z P. A precipitation-hardened high-entropy alloy with outstanding tensile properties [J]. Acta Materialia, 2016, 102: 187−196.
[46] HE J Y, ZHU C, ZHOU D Q, LIU W H, NIEH T G, LU Z P. Steady state flow of the FeCoNiCrMn high entropy alloy at elevated temperatures [J]. Intermetallics, 2014, 55: 9−14.
[47] COURTNEY T H. Mechanical behavior of materials [M]. Waveland: Long Grove, 2005.
[48] KOZLOV E V, ZHDANOV A N, KONEVA N A. Barrier retardation of dislocations. Hall−Petch problem [J]. Physical Mesomechanics, 2006, 9(3): 75−85.
[49] LIU W H, WU Y, HE J Y, NIEH T G, LU Z P. Grain growth and the Hall−Petch relationship in a high-entropy FeCrNiCoMn alloy [J]. Scripta Materialia, 2013, 68(7): 526−529.
[50] OTTO F, DLOUHÝ A, SOMSEN C, BEI H, EGGELER G, GEORGE E P. The influences of temperature and microstructure on the tensile properties of a CoCrFeMnNi high-entropy alloy [J]. Acta Materialia, 2013, 61(15): 5743−5755.
[51] SRIHARITHA R, MURTY B S, KOTTADA R S. Alloying, thermal stability and strengthening in spark plasma sintered $Al_xCoCrCuFeNi$ high entropy alloys [J]. Journal of Alloys and Compounds, 2014, 583: 419−426.
[52] RAMESH K T. Nanomaterials mechanics and mechanisms [M]. New York: Springer, 2009.
[53] LI Xiao-yan, WEI Yu-jie, LU Lei, LU Ke, GAO Hua-jian. Dislocation nucleation governed softening and maximum strength in nano-twinned metals [J]. Nature, 2010, 464(8): 877−880.
[54] YANG Yu-long, LIANG Yi-long, HE Guan-yu, LUO Ping-xi. Simultaneously enhancing the strength, plasticity, and conductivity of copper matrix composites with graphene-coated submicron spherical copper [J]. Nanomaterials-Basel, 2022, 12(6): 1025.
[55] VITTORI M, MIGNONE A. On the antiphase boundary energy of $Ni_3(Al,Ti)$ particles [J]. Materials Science and Engineering, 1985, 74(1): 29−37.
[56] WANG Y P, LI B S, REN M X, YANG C, FU H Z. Microstructure and compressive properties of AlCrFeCoNi high entropy alloy [J]. Materials Science and Engineering: A, 2008, 491(1/2): 154−158.
[57] ZUO T T, LI R B, REN X J, ZHANG Y. Effects of Al and Si addition on the structure and properties of CoFeNi equal atomic ratio alloy [J]. Journal of Magnetism and Magnetic Materials, 2014, 371: 60−68.
[58] WANG X F, ZHANG Y, QIAO Y, CHEN G L. Novel microstructure and properties of multicomponent CoCrCuFeNiTi_x alloys [J]. Intermetallics, 2007, 15: 357−362.

烧结温度对 $Co_{1.5}CrFeNi_{1.5}Ti_{0.6}$ 高熵合金组织演变和性能的影响

王 超[1]，安维峥[2]，马 强[2]，王 香[1]，李嘉欣[1]，梁朝阳[1]，聂其东[3]

1. 哈尔滨工程大学 超轻材料与表面技术教育部重点实验室，哈尔滨 150001；
2. 中海油研究总院有限责任公司，北京 100028；
3. 青岛理工大学 机电工程系，临沂 273400

摘 要：为开发一种具有优异力学性能和耐腐蚀性能的海洋工程材料，采用机械合金化和放电等离子烧结技术制备一种新型非等原子 $Co_{1.5}CrFeNi_{1.5}Ti_{0.6}$ 高熵合金。结果表明，由于金属原子的扩散速率、均匀化和明显的迟滞扩散效应，烧结温度对高熵合金的显微组织和相组成有显著影响。烧结温度低于 1050 ℃时，高熵合金主要由面心立方(FCC)、$Ni_3Ti(\varepsilon)$、$Ni_{2.67}Ti_{1.33}(R)$和 Fe−Cr(σ)相组成。合金的显微组织由粗大的枝晶结构组成，其含量和尺寸都随着烧结温度的升高而逐渐减小。然而，在 1100 ℃以上烧结的高熵合金则只含有细小的等轴晶。在 1100 ℃下烧结的高熵合金只含有 FCC 固溶体，而烧结温度超过 1150 ℃时，ε 相会在 FCC 基体内析出。烧结温度为 1050 ℃时，高熵合金的显微组织由短棒状枝晶和细小等轴晶组成。由于沉淀强化和晶界强化的影响，这种合金的屈服强度最高，达到 1198.71 MPa。同时，1050 ℃以上烧结的高熵合金还表现出优异的耐腐蚀性。考虑到显微组织、力学性能和腐蚀性能，1050 ℃被确定为 $Co_{1.5}CrFeNi_{1.5}Ti_{0.6}$ 高熵合金的最佳烧结温度。

关键词：$Co_{1.5}CrFeNi_{1.5}Ti_{0.6}$ 高熵合金；耐腐蚀性能；显微组织演变；烧结温度；强化机理

(Edited by Xiang-qun LI)